Parallel pathways for rapid odor processing in lateral entorhinal cortex: Rate and temporal coding by layer 2 subcircuits.

Sebastian H. Bitzenhofer[1,2,*], Elena A. Westeinde[1], Han-Xiong Bear Zhang[1] & Jeffry S. Isaacson[1,*,#],

[1]Center for Neural Circuits and Behavior and Department of Neurosciences, University of California, San Diego, La Jolla, CA 92093, USA
[2]Current address: Institute of Developmental Neurophysiology, Center for Molecular Neurobiology, University Medical Center Hamburg-Eppendorf, 20251 Hamburg, Germany

*Correspondence:
Jeffry S. Isaacson or Sebastian H. Bitzenhofer
Center for Neural Circuits and Behavior, Rm.213
9500 Gilman Dr.
La Jolla, CA 92093-0634, USA
jisaacson@ucsd.edu
858-822-3526

[#]Lead Contact:
Jeffry S. Isaacson

Author Contributions:
S.H.B. and J.S.I. designed the project. S.H.B. conducted and analyzed *in vivo* experiments. E.A.W., H.-Z. B. Z., and J.S.I. conducted and analyzed slice experiments. S.H.B. and J.S.I. wrote the manuscript.

Acknowledgements
We are grateful to B. Nguyen for mouse training and technical support. We thank Fan Wang for providing NetrinG1-cre mice. S.H.B. is a WBP Fellow (DFG, German Research Foundation) - 445900988. H.-Z. B. Z. was a member of the UCSD-ZJU SRTP Program. This work was supported by NIH R01DC04682 and R01DC015239.

Summary

Olfactory information is encoded in lateral entorhinal cortex (LEC) by two classes of layer 2 (L2) principal neurons: fan and pyramidal cells. However, the functional properties of L2 neurons are unclear. Here, we show in awake mice that L2 cells respond rapidly to odors during single sniffs and that LEC is essential for discrimination of odor identity and intensity. Population analyses of L2 ensembles reveals that while rate coding distinguishes odor identity, firing rates are weakly concentration-dependent and changes in spike timing represent odor intensity. L2 principal cells differ in afferent olfactory input and connectivity with local inhibitory circuits and the relative timing of pyramidal and fan cell spikes underlies odor intensity coding. Downstream, intensity is encoded purely by spike timing in hippocampal CA1. Together, these results reveal the unique processing of odor information by parallel LEC subcircuits and highlight the importance of temporal coding in higher olfactory areas.

Introduction

Olfactory cues provide rich information about the environment critical for behaviors as diverse as food seeking, social interactions, and predator avoidance. These behaviors depend not only on the identification of specific odors, but also on the detection of odor concentration which is essential for odor-guided navigation (Ache et al., 2016; Marin et al., 2021). In mammals, olfactory information is initially encoded by the firing activity of olfactory bulb (OB) mitral cells (Uchida et al., 2014; Wilson and Mainen, 2006). This information projects directly via the lateral olfactory tract (LOT) to the primary olfactory (piriform) cortex (PCx), a region thought to be critical for odor perception (Blazing and Franks, 2020; Uchida et al., 2014; Wilson and Sullivan, 2011). Although the properties of circuits in OB and PCx governing olfaction have

received considerable attention, much less is known about odor processing in higher brain areas. In this study, we explore the nature of odor coding in lateral entorhinal cortex (LEC), a higher region that transmits information to the hippocampus which underlies odor-dependent memories and navigation (Li et al., 2017; Radvansky and Dombeck, 2018).

The LEC receives two main sources of olfactory input: direct projections from OB mitral cells via the LOT and indirect projections via PCx principal cells (Haberly and Price, 1978; Kerr et al., 2007). These inputs synapse onto two distinct types of L2 principal neurons: fan and pyramidal cells (Canto and Witter, 2012; Kobro-Flatmoen and Witter, 2019; Tahvildari and Alonso, 2005). Fan cells in L2a have extensive apical dendritic arbors but lack basal dendrites, express reelin, and project via the lateral perforant path to granule cells in the dentate gyrus (Leitner et al., 2016; Vandrey et al., 2020). Pyramidal cells are concentrated in L2b, express calbindin, project to stratum lacunosum moleculare (SLM) of hippocampal CA1 and send feedback projections to the PCx and olfactory bulb (Chapuis et al., 2013; Leitner et al., 2016). LEC neurons respond in an odor-specific fashion (Leitner et al., 2016; Woods et al., 2020; Xu and Wilson, 2012) and calcium imaging in anesthetized mice revealed that fan cells respond more selectively to odors than pyramidal cells (Leitner et al., 2016). However, the role of LEC in odor discrimination as well as the coding of odor identity and intensity by fan and pyramidal cells in awake animals have not been established.

Rodents can make odor-guided behavioral decisions based on neural activity triggered by a single sniff (Chong and Rinberg, 2018; Uchida and Mainen, 2003) and studies have shed light on odor coding features of the OB and PCx. Odor identity is represented by the spatiotemporal activity patterns of OB mitral cells (Bathellier et al., 2008; Chong and Rinberg, 2018; Cury and Uchida, 2010; Shusterman et al., 2011) and the spike timing of cells early after

odor inhalation is especially important for odor discrimination (Chong et al., 2020; Gill et al., 2020; Wilson et al., 2017). Changes in odor concentration can be decoded from both spike rate and the temporal profile of odor-evoked responses (Bathellier et al., 2008; Cang and Isaacson, 2003; Margrie and Schaefer, 2003; Sirotin et al., 2015). In PCx, odor identity is represented by distributed ensembles of active layer 2/3 pyramidal cells (Blazing and Franks, 2020; Schoonover et al., 2021; Stern et al., 2018; Stettler and Axel, 2009; Uchida et al., 2014). Recent work indicates that odor identity is encoded by ensembles of pyramidal cells active early during individual sniffs in a manner invariant to odor concentration (Bolding and Franks, 2018). In contrast, odor intensity can be determined from a subpopulation of later responding pyramidal cells whose firing latencies shift earlier as odor concentration increases (Bolding and Franks, 2017).

In this study, we use extracellular recordings in awake mice, odor-driven behavior, and brain slice experiments to determine how LEC L2 principal cells contribute to olfactory information processing.

Results

Early odor-evoked activity during single sniffs in LEC

Previous work revealed distinct differences in the timing of odor-evoked activity in the OB and PCx during individual sniffs. While OB mitral cells fire spikes at odor-specific latencies that tile individual respiration cycles (Bathellier et al., 2008; Cury and Uchida, 2010; Shusterman et al., 2011), PCx pyramidal cells preferentially fire within the first 100 ms of odor inhalation (Bolding and Franks, 2018). However, the timing of odor-evoked activity in LEC relative to respiration-coupled firing in the OB and PCx is unknown. To address this question, we made simultaneous recordings of multi-unit activity using silicon probes in the OB mitral cell layer,

L2/3 of anterior PCx, and L2 of LEC (Supplemental Fig. 1B) in awake, head-fixed mice (Fig. 1A$_1$). We monitored nasal airflow at the outlet of a custom built olfactometer and delivered monomolecular odors (n=11) triggered by the exhalation phase of respiration (respiration cycle duration ~300 ms, Supplemental Fig. 1A). This approach allowed us to precisely align all recordings to the onset of the first inhalation of the applied odor for each trial (Fig. 1A$_2$). Consistent with recent findings (Bolding and Franks, 2018), while odors evoked OB mitral cell activity during both early and late phases of a sniff (peaks at 43 ms and 232 ms, respectively, n= 6 mice), responses in PCx selectively occurred early (peak time 53 ms) after odor inhalation (Fig. 1B). Interestingly, we found that simultaneously recorded activity in LEC also preferentially occurred early after odor inhalation (peak at 75 ms, Fig. 1B). Experiments using channelrhodopsin-driven firing of OB mitral cells revealed similar shifts in the timing of early activity from OB to LEC suggesting that increasing latencies largely reflect axonal conduction times across regions (Supplemental Fig. 1C).

We isolated single units to further explore the timing of odor-evoked activity across individual cells in the three brain regions (Fig. 1C). While individual OB mitral cells showed odor-evoked responses that peaked at times that tiled the entire respiration cycle, many L2/3 PCx and L2 LEC cells preferentially responded early after odor inhalation (Figs. 1C, 1D$_{1\text{-}2}$). Overall, the percentage of significantly activated cells per odor during the early phase of respiration (<100 ms after inhalation) was greater in the PCx and LEC compared to the OB (Fig. 1D$_3$). In contrast, across the three olfactory areas, the fraction of activated cells per odor during later times (200-300 ms post-inhalation) was lowest for the LEC. Together, these results suggest that activity triggered early during individual sniffs is import for odor coding in LEC.

Behavioral discrimination of odor identity and intensity requires the LEC

The importance of the LEC in odor-driven behavior has yet to be established. To test this, we took advantage of an optogenetic approach to acutely silence the LEC in head-fixed mice performing odor discrimination in a two-alternative forced-choice (2AFC) task (Fig. 2A). Transgenic mice (GAD2-cre x Ai32) selectively expressing ChR2 in inhibitory neurons were trained (>75% correct responses) to lick left or right to distinguish odor identity (isoamyl acetate vs limonene, both at 1% concentration). For each trial (≥4 s interval), odor application (1 s duration) began at the respiration exhalation phase so that behavior could be aligned to the onset of the first inhalation of each odor. Mice were free to report their choice (left or right lick) at any time within 2 s of odor onset and fiber-coupled LEDs (473 nm) targeting the LEC bilaterally were used to suppress cortical activity during odor delivery on a random subset (25%) of trials. We found that LEC is critical for discrimination of odor identity since LEC silencing reduced the fraction of correct responses to the chance level (Fig. 2B, LED off: 83.76 ± 3.17%, LED on: 57.06 ± 5.22%, p=0.009, paired t-test). Moreover, by analyzing lick timing, we determined that mice could discriminate the two odors by as early as 225 ms after inhalation onset (Fig. 2B, Supplemental Figs. $2A_{2\text{-}3}$). This rapid behavioral discriminability is consistent with the rapid timing of odor-evoked activity we observe in LEC, especially when considering motor initiation delays.

We next tested whether LEC played a role in the behavioral discrimination of odor intensity. Mice performed the same 2AFC task, but were trained to distinguish two different concentrations of the same odor (0.25% vs. 1.0% ethyl tiglate, Fig. 2C). Silencing LEC again reduced the fraction of correct responses to the chance level (LED off: 77.40 ± 1.58%, LED on: 52.37 ± 2.10%, p=0.0003, paired t-test), indicating that the LEC is also essential for detecting odor intensity and analysis of lick times revealed that mice could perform this discrimination

rapidly (175 ms following odor inhalation, Fig. 2C, Supplemental Figs. $2B_2$, $2B_3$). Control experiments confirmed that the effects of LED illumination during odor discrimination were specifically due to cortical silencing (Supplemental Fig. $2A_1$, $2B_1$, 2C, 2D). Together, these findings indicate that LEC plays an essential role in behavior requiring discrimination of odor identity or intensity. Furthermore, the rapid speed of LEC-dependent behavior during single sniffs is entirely consistent with the rapid time course of odor-evoked activity we observe in L2.

Ensemble coding of odor identity in LEC

We examined how the activity of L2 neurons encodes odor identity in LEC by analyzing responses of individual cells to the panel of 11 odorants (Fig. 3A). Across all individual cells (n=576), odor-evoked firing peaked in a time window 50-100 ms from the start of odor inhalation, considerably earlier than respiration-coupled activity observed in the absence of applied odor (blank response, Fig. 3B). We thus used this 50 ms time window for analysis of rapid odor evoked activity in LEC. Individual odors activated overlapping ensembles of L2 neurons with 48% of cells showing increases in firing rate to two or more odors (Fig. $3C_1$). Sorting responses of significantly activated cells normalized to the odors causing their strongest activation revealed that cells respond strongly to few preferred odors, whereas the least preferred odors actually suppressed activity (Fig. $3C_2$).

To study how activity in populations of L2 neurons might be used to encode odor identity, we used principal component analysis (PCA) of trial-by-trial response vectors from firing activity of all neurons recorded for each odor (see Methods). Vectors were binned in 1 ms intervals to examine the trajectory of the first three principal components following odor inhalation. Responses rapidly became more dispersed (discriminable) in PCA space (i.e. 0 ms vs.

75 ms post-inhalation onset) and reverted to the pre-odor condition by 200 ms (Fig. 3D$_1$). We measured discriminability using the Euclidean distance in PCA space for the different odors. This confirmed that the biggest difference in population activity occurred during the early peak of LEC odor-evoked activity (Fig. 3D$_2$). We next trained a linear classifier to test the ability to decode odor identity from population activity. Using a sliding time window (integrating 50 ms of activity every 5 ms), the classifier distinguished odor identities with high accuracy (>90 %) within 100 ms of odor inhalation (Fig. 3D$_3$). We found an equally high accuracy in odor identification when cells were characterized only based on whether they showed significant increases in firing rate (Fig. 3D$_3$). Thus, simply knowing which cell ensembles are active across the population provide as much information about odors as cell firing rates. While decoding accuracy remained high over the duration of the respiration cycle, reducing the integration time window for the linear classifier revealed a more transient increase in accuracy locked to the early phase of odor inhalation (Supplemental Fig. 3A$_1$-$_2$). This indicates that LEC population activity during later phases of individual sniffs contains information about odor identity only if activity is integrated over extended time windows. Classifier performance specifically during the rapid peak of odor-evoked activity (50-100 ms post-inhalation) improved as the population of cells used for classification increased (Supplemental Fig. 3B), however, high levels of accuracy (>50%) were readily achieved with ensembles of <250 L2 neurons (Supplemental Fig. 3B).

Spike timing in LEC encodes odor intensity

Does early odor-evoked activity in LEC also contain information regarding odor intensity? To address this question, we analyzed activity of single L2 neurons in response to four concentrations (0.25, 0.33, 0.50, 1.00%) of the same set of 11 odors. Individual cells had diverse patterns of responses to different odor concentrations, with some showing a simple scaling of

firing rate as odor concentration increased while others showed concentration-dependent changes in the time course of the evoked response (Fig. $4A_1$). Averaging odor-evoked activity across all units revealed only a weak increase in early firing rate for a 4-fold change in odor concentration (50-100 ms post-inhalation, 0.8-fold increase, $\rho = 0.3$, $p = 0.03$, Spearman's rank correlation, Fig. $4A_2$, Supplemental Fig. $4A_2$). Similarly, we found only a modest increase in the percentage of activated cells per odor as concentration increased ($\rho = 0.3$, $p = 0.05$, Spearman's rank correlation, Supplemental Fig. $4A_1$) and lifetime sparseness (a measure of response selectivity) was weakly sensitive to changes in concentration ($\rho = 0.04$, $p = 0.04$, Spearman's rank correlation, Supplemental Fig. $4A_3$). These findings suggest that odor intensity might not be optimally represented by the firing rates of ensembles of LEC neurons.

We used PCA of the pseudo-population activity grouped by odor concentration to understand how responses evolved over the time course of single sniffs. Interestingly, responses to the four concentrations rapidly dispersed in PCA space after odor inhalation and returned to pre-odor levels of variability within 200 ms (Fig. $4B_1$). This suggests that ensemble activity based on early odor-evoked changes in firing rate could be used to discriminate odor intensity. Indeed, the Euclidean distances in PCA space between responses to different odor concentrations revealed a clear peak within 100 ms of odor inhalation (Fig. $4B_2$). However, these values were much less than those obtained from PCA comparing different odors and increasing concentration only slightly increased the distances that distinguished between odors (Fig. $4B_2$). Thus, population activity showed smaller differences (less discriminability) between odor concentrations when compared to activity representing different odor identities.

We trained a linear classifier to detect odor identity for the different concentrations using firing rates integrated over a sliding 50 ms window. Classification accuracy of odor identity only

slight improved as concentration increased (Figs. 4C$_{1-2}$, Supplemental Fig. 4B$_1$). In contrast, when we trained the linear classifier to detect odor concentration based on firing rate, classification accuracy was considerably worse (Fig. 4C$_3$, Supplemental Fig. 4B$_2$). Indeed, classification accuracy for each of the 11 tested odors was only marginally above chance level (Fig. 4C$_4$). Taken together, these findings suggest that rate coding provides a relatively poor basis for representing information regarding odor intensity in LEC.

What other properties of evoked activity might underlie the representation of odor intensity in LEC? When studying odor-evoked responses at higher temporal resolution, we found that the average time to peak firing of L2 cells shifted earlier as odor concentration increased (Fig. 4D$_1$). We quantified this shift by determining the time of peak firing (relative to odor inhalation) for all cell-odor pairs across odor concentrations and found that peak times shifted earlier with increasing odor concentrations ($\rho = -0.04$, $p < 0.001$, Spearman's rank correlation, Fig. 4D$_2$). We next considered the possibility that changes in spike timing across the L2 cell population altered the relative synchrony of odor-evoked activity in LEC. Indeed, pairwise peak time differences for odor responses became smaller as odor concentration increased ($\rho = -0.03$, $p < 0.001$, Spearman's rank correlation, Fig. 4D$_3$, Supplemental Fig. 4C$_{1-2}$). This indicates that activity in LEC becomes more synchronized with increases in odor concentration. Together, these findings show that odor intensity can be distinguished using a temporal code in LEC.

Differential connectivity of fan and pyramidal cells with long range and local circuits

How do the two types of L2 principal neurons contribute to odor processing in LEC? We first used brain slices to study the functional properties of L2 fan and pyramidal cells. We took advantage of the fact that the two cell types can be distinguished by their distinct axonal

projection patterns: fan cells project to DG granule cells while L2 pyramidal cells send feedback projections to the OB (Chapuis et al., 2013; Leitner et al., 2016; Vandrey et al., 2020). We injected green Retrobeads into either the DG or OB and made targeted whole-cell current clamp recordings from bead-labeled cells in coronal LEC slices. In a subset of experiments, we used mice that express red fluorescent protein in olfactory cortical pyramidal cells (Ntsr1-cre x Ai14, (Boyd et al., 2012)) Biocytin was added to the pipette internal solution for post-hoc reconstruction of dendritic arbors. DG bead injection labeled neurons with cell bodies localized in L2a (Fig. $5A_1$) that possessed extensive, fan-like apical dendrites but few basal dendrites (Fig. $5A_2$, Supplemental Fig. 5A). In contrast, OB injection labeled cells in L2b (Fig. $5B_1$) with typical pyramidal cell dendritic morphology (Fig. $5B_2$, Supplemental Fig. 5A). Similar to previous studies of L2 fan and pyramidal cells (Leitner et al., 2016; Tahvildari and Alonso, 2005; Vandrey et al., 2020), current injection revealed differences in membrane excitability including resting potential (fan: -64 ± 1.1 mV (n=15), pyramidal: -69.4 ± 1.7 mV (n=10), p = 0.016, t-test), input resistance (fan: 147.6 ± 10.4 mOhm, pyramidal: 102.1 ± 12.8 mOhm, p = 0.012), and sag (fan: 3.7 ± 0.4 mV, pyramidal: 1.1 ± 0.4 mV, p = 0.0003).

We next used an optogenetic approach to examine whether fan and pyramidal cells differed in their olfactory input. To probe direct input from the OB, we took advantage of Tbet-cre mice crossed with the Ai32 reporter line to selectively express ChR2 in OB mitral cells (Haddad et al., 2013). We used LEC slices from these mice to make simultaneous voltage-clamp recordings (-70 mV) from L2a fan and L2b pyramidal cells (Fig. $5C_1$) that were confirmed by posthoc anatomical reconstruction. Excitatory postsynaptic currents (EPSCs) evoked from ChR2-expressing LOT fibers (473 nm, 4 ms flash) were significantly larger in fan vs. pyramidal cells (Fig. $5C_2$, 136.7 ± 3 pA and 22.3 ± 5.5 pA, respectively, n=7 pairs, p=0.02, paired t-test).

Paired-pulse facilitation (200 ms interstimulus interval) was identical for fan and pyramidal cell EPSCs (Supplemental Fig. 5B, paired pulse ratio 1.9 ± 0.2 and 1.8 ±0.3, respectively, p=0.69, paired t-test) suggesting that LOT release probability was the same onto both cell types. Moreover, the amplitude of single fiber EPSCs recorded in fan (n=8) and pyramidal (n=7) cells using minimal LOT stimulation were also virtually identical (Supplemental Fig. 5C, 9.7 ± 1.7 pA and 7.9 ± 1.1 pA, respectively, p=0.35, t-test). These results indicate that the stronger LOT-evoked responses of fan cells reflect the fact that they receive inputs from more OB mitral cells than pyramidal cells. Projections from piriform cortex provide another source of olfactory input to the LEC. To study these inputs, we used LEC slices from mice injected in anterior PCx with adeno-associated virus (AAV) driving expression of ChR2. A subset of experiments were performed in the presence of tetrodotoxin (1 μM) and 4-aminopyridine to ensure monosynaptic input (Petreanu et al., 2009). Simultaneous recordings revealed larger ChR2-evoked EPSCs in fan vs. pyramidal cells (Fig. 5D, 331 ± 41.4 pA and 174 ± 22.6 pA, respectively, n=15 pairs, p=0.002, paired t-test) indicating that fan cells also receive stronger olfactory input relayed from the piriform cortex.

In addition to olfactory excitatory input, we considered the possibility that fan and pyramidal cells might differ in their inhibition by local GABAergic interneurons. We addressed this by studying the impact of two major classes of inhibitory interneurons: soma-targeting, parvalbumin (PV) cells and dendrite-targeting somatostatin (SOM) cells (Isaacson and Scanziani, 2011). We made simultaneous recordings of inhibitory postsynaptic currents (IPSCs, V_m= 0 mV) from fan and pyramidal cells using LEC slices from PV-cre (Fig. 5E) or SOM-cre mice (Fig. 5F) crossed with a ChR2 reporter line (Ai32). We drove interneuron firing with different durations of LED illumination (2-32 ms) and fit the relationship between LED duration

and inhibitory charge with a line to compare the slopes of the input/output relationship for each cell pair. Interestingly, these experiments revealed that fan cells received substantially less inhibition from PV cells than pyramidal cells (Fig. 5E) while both cell types received the same relative amount of SOM cell-mediated inhibition (Fig. 5F). Thus, fan and pyramidal cells also differ in their connectivity with local interneuron circuits.

Temporal shift of pyramidal cell firing relative to fan cells regulates synchronous activity

The differences in olfactory input and PV-cell mediated inhibition between L2 fan and pyramidal cells suggest that the two principal cells may respond heterogeneously to odors. To investigate this idea, we identified cre mouse lines that could be used to target *in vivo* recordings to the different L2 principal cell types. We found that NetrinG1-cre mice, which selectively label semilunar principal cells in PCx, (Bolding et al., 2020) specifically targeted fan cells in LEC. In NetrinG1-cre x Ai14 mice, TdTomato-expressing cells localized to L2a and were co-labeled by retrobeads injected in the DG (Fig. $6A_1$, 90.47 ± 1.47%, n=6 slices from 3 mice). Furthermore, immunolabeling revealed that NetrinG1-cre expression was restricted to reelin-positive neurons in LEC L2a and did not overlap with L2b cells expressing calbindin (Supplemental Fig. 6A). To target recordings to L2 pyramidal cells, we used Calbindin-cre mice (Leitner et al., 2016). We confirmed that cells expressing Calbindin-cre were concentrated in L2b, co-labeled by retrobeads injected in the OB (81.89 ± 2.39%, n=6 slices from 3 mice), and immuno-positive for calbindin but not reelin (Fig. $6A_2$, Supplemental Fig. 6B). Although calbindin is also expressed in some GABAergic neuron subtypes, calbindin immunolabeling in GAD2-cre x Ai14 mice revealed very few calbindin-positive interneurons in LEC (Supplemental Fig. 6C).

We crossed NetrinG1-cre and Calbindin-cre mice with Ai32 mice to express ChR2 in LEC L2 fan and pyramidal cells, respectively, and used photo-tagging (Lima et al., 2009) to identify the cell types during single-unit recording in awake, head-fixed mice (Supplemental Fig, 6D). Both identified cell types showed an early peak of odor-evoked activity (Fig. 6B, 6C) and we found only modest differences in ensemble coding of odor identity; the number of activated units per odor and mean evoked firing rate was slightly greater for pyramidal cells while lifetime sparseness (a measure of odor selectivity) was higher for fan cells (Supplemental Fig. $6E_{1\text{-}3}$).

In contrast to the subtle distinctions in odor identity coding, we found a notable difference in how changes in odor concentration modulated spike timing in fan and pyramidal cells. While the average latency to peak response shifted earlier as concentration increased for pyramidal cells, the time course of fan cell responses appeared concentration invariant (Fig. 6D). We confirmed this by quantifying the peak responses for all cell-odor pairs. We found that although peak firing rates slightly increased with odor concentration for both cell types (fan: $\rho = 0.04$, $p = 0.009$, pyramidal: $\rho = 0.04$, $p = 0.010$, Spearman's rank correlation, Fig. $6E_1$), they differed significantly in how odor concentration modulated spike timing: time to peak firing for pyramidal cells became faster as concentration increased, whereas fan cell peak firing times were largely unaffected (fan: $\rho = -0.02$, $p = 0.22$, pyramidal: $\rho = -0.09$, $p < 0.001$, Spearman's rank correlation, Fig. $6E_2$). Interestingly, the peak firing times of fan cells typically preceded pyramidal cells (Fig. $6E_2$) and pyramidal, but not fan cells, fired more synchronously as odor concentration increased (fan: $\rho = -0.0002$, $p = 0.73$, pyramidal: $\rho = -0.007$, $p < 0.001$, Spearman's rank correlation, Supplemental Fig. $6E_4$). The temporal shift in pyramidal cell activity and earlier (but constant) timing of fan cell responses underlies spike synchronization between the cell types as odor concentration increases ($\rho = -0.05$, $p < 0.001$, Spearman's rank correlation, Fig. $6E_3$).

Together, these results show that relative differences in spike timing between fan and pyramidal cells underlie the temporal coding of odor intensity in LEC L2.

A purely temporal code for odor intensity in CA1

Spike timing and synchrony in L2 of LEC provides a potential mechanism for odor intensity coding, but is this information relevant downstream in the hippocampus? To probe how information from LEC was routed to the hippocampal formation, we first traced the projections from L2 principal cells by injecting AAV1-CAG-FLEX-tdTomato into the LEC of NetrinG1-cre and Calbindin-cre mice (Fig. 7A). This showed that fan cells send dense input to the outer molecular layer of the DG via the lateral perforant path ((Leitner et al., 2016; Vandrey et al., 2020), Fig. 7A$_1$). Injections in Calbindin-cre mice revealed projections from L2 pyramidal cells to hippocampal CA1 through the temporoammonic pathway ((Amaral and Witter, 1989; Kitamura et al., 2014; Masurkar et al., 2017), Fig. 7A$_2$). This tracing confirmed that information from LEC L2 is relayed to CA1 via both direct (pyramidal cell) and indirect (fan cell) pathways.

We next used linear silicon probes to record odor-evoked activity in intermediate CA1 in awake, head-fixed mice. Like PCx and LEC, cells in CA1 preferentially responded early during individual sniffs (Fig. 7B$_{1\text{-}2}$) and peak odor-evoked firing in CA1 (106 ms, odor concentration 1%) occurred briefly after LEC fan (72 ms) and pyramidal (78 ms) cells. Surprisingly, in contrast to LEC L2, the peak firing rate in CA1 was insensitive to odor concentration (Fig. 7B$_2$ compared to Fig. 4A$_2$). Unlike LEC, the percentage of activated cells per odor, mean firing rate, and response sparseness were also concentration independent in CA1 (Supplemental Fig. 7A$_{1\text{-}3}$). This suggests that rate coding features found in LEC that could contribute to odor intensity discrimination are discarded at the level of CA1. Indeed, although PCA (Supplemental Fig. 7A$_4$)

and the use of linear classifiers revealed that odor identity could be distinguished with high accuracy (Fig. 7B$_3$, Supplemental Fig. 7B$_1$), odor intensity could not be decoded from CA1 firing rates (Fig. 7B$_4$, Supplemental Figs. 7A$_4$, 7B$_2$). Thus, firing rates contain information about odor identity, but not intensity in CA1.

Importantly, we observed that the timing of early odor-evoked activity was dependent on concentration in CA1 (Fig. 7C$_1$). Although peak firing rate was concentration insensitive, the time to peak shifted earlier as concentration increased (peak rate: $\rho = -0.002$, $p = 0.7$, peak time: $\rho = -0.04$, $p < 0.001$, Spearman's rank correlation, Fig. 7C$_2$-$_3$). As we found for LEC, pairwise peak time differences were reduced with increasing odor concentration indicating that firing also became more synchronized within CA1 ($\rho = -0.01$, $p < 0.001$, Spearman's rank correlation, Fig. 7C$_4$, Supplemental Fig. 7B$_3$). These findings indicate that downstream of LEC, odor intensity must ultimately be represented by changes in spike timing in CA1.

Discussion

In this study, we examined olfactory information processing in the LEC of awake mice. We found that odors activate principal L2 cells early during individual sniffs and that LEC is essential for rapid odor-guided behavior. Odor identity was readily decoded from the firing rates of ensembles of L2 cells but firing rate was suboptimal for discerning odor intensity. Instead, changes in odor concentration were well described by shifts in the timing and synchrony of spikes. We found that the two types of L2 principal neurons, fan and pyramidal cells, differ in their functional properties. Slice recordings revealed stronger olfactory input and weaker PV cell inhibition of L2 fan cells compared to pyramidal cells and targeted *in vivo* recordings showed that spike timing differences between the cell types underlie odor intensity coding in LEC.

Interestingly, we found that CA1 discards any concentration-dependent firing rate changes inherited from LEC and represents odor intensity using a purely temporal code.

In awake animals, the timing of respiration-coupled activity driven by odors varies across brain regions. While population activity of OB mitral cells spans individual respiration cycles, L2/3 pyramidal cells in PCx respond to odors preferentially early after odor inhalation (Bolding and Franks, 2018; Shusterman et al., 2011). Recurrent inhibition has been found to enforce the short time window for sniff-coupled activity elicited by odors in PCx (Bolding and Franks, 2018). Here we show in LEC, which receives input from both the OB and PCx, that odor-evoked activity is also largely limited to an early window within 100 ms of odor inhalation. Like PCx, local feedback inhibition presumably curtails late odor-evoked activity in LEC.

We found that optogenetic suppression of the LEC abolished rapid behavioral discrimination of odor identity and intensity, indicating that the LEC is essential for odor-guided behavior. Mice made decisions during the 2AFC task using information obtained early during single sniffs of odor. Thus, it is likely that L2 activity early during individual sniffs is critical for odor-driven behavior. Our experiments required simple discrimination of markedly different odorants or odor concentrations; we do not rule out the possibility that mice could integrate LEC activity over longer periods (even across multiple sniffs) during tasks requiring more difficult odor discrimination.

Given the timing of odor-guided behavior and odor-evoked activity in LEC, we studied how information regarding odor identity is encoded by rapid L2 cell responses. We find that different odors are represented by overlapping ensembles of active cells in LEC, similar to odor coding in PCx (Blazing and Franks, 2020; Poo and Isaacson, 2009; Stettler and Axel, 2009;

Uchida et al., 2014). Population analyses established that a firing rate code distinguished odor identity in L2 and distinct odor representations emerged rapidly (<100 ms) after inhalation. Interestingly, as in PCx (Bolding and Franks, 2017), simply knowing whether cells were activated or not by odors was as effective as knowing actual firing rates when decoding odor identity from population activity.

Increases in odor concentration over a 4-fold range caused modest increases in firing rate of L2 cells and population analyses revealed that increases in concentration could improve discrimination of odor identity. However, for individual odors, changes in firing rate worked poorly for decoding odor intensity from population activity. Instead, we found that increases in concentration shifted the times of peak odor responses earlier during individual sniffs and spiking became more synchronized across cells. In anterior PCx, odor representations were reported to be "concentration-invariant" when rapid population responses were studied using firing rates (Bolding and Franks, 2018). On the other hand, a subpopulation of PCx neurons whose latencies decreased as odor concentrations increased have been suggested to provide a temporal code for odor intensity (Bolding and Franks, 2017). In LEC, firing rate provides some information, albeit limited, for determining odor intensity from population activity. However, temporal features of the population response well represent intensity in LEC.

We studied LEC L2 microcircuits in more detail using voltage-clamp clamp recordings in brain slices. We found that the L2 principal neuron subtypes, fan and pyramidal cells, differed in their local and long-distance inputs. Fan cells receive contacts from more OB mitral cells than pyramidal cells. PCx inputs are also stronger onto fan cells. One simple explanation for these differences is the fact that fan cells have more extensive apical dendrites spreading through L1, where inputs converge from LOT and PCx. Intriguingly, fan cells also received markedly weaker

inhibition from PV cells. This suggests that odors may produce stronger afferent excitation and weaker somatic inhibition in fan vs. pyramidal cells. Interestingly, a study using paired recordings to examine local connectivity in LEC slices (Nilssen et al., 2018) reported that fast spiking cell connectivity was more prevalent with fan (17 connections of 28 pairs, 61%) than pyramidal cells (3 of 11, 27%). Differences in the approach for targeting interneurons (genetic targeting (ours) vs. electrophysiological properties (Nilssen et al., 2018)) could account for the apparent discrepancy between the studies.

We studied odor-evoked responses of fan and pyramidal cells using optogenetic tagging in cre mice. If connections from OB mitral cells to LEC are distributed "randomly" as proposed for the PCx (Schaffer et al., 2018; Sosulski et al., 2011; Stettler and Axel, 2009) the fact that fan cells receive more LOT input than pyramidal cells suggests that they might be more broadly tuned for odors. However, we found odor representations were actually sparser for fan compared to pyramidal cells. This observation is consistent with a recent calcium imaging study reporting that fan cells are more odor selective than pyramidal cells (Leitner et al., 2016). Given the smaller size of the LOT at the level of the LEC, odor representations here are presumably less influenced by direct OB input than PCx. More studies examining the distribution of OB inputs in the LEC would help understand tuning properties in this region.

We found marked differences in the timing of sniff-coupled responses in fan and pyramidal cells as odor concentration changed. Fan cells always responded earlier than pyramidal cells and their peak response times were largely concentration-invariant. In contrast, the peak response times of pyramidal cells consistently shifted earlier as concentration increased. The net effect was a concentration-dependent increase in the synchrony of spiking between the two cell populations. We suspect that the stronger olfactory input and weaker PV inhibition onto

fan cells, rather than broadening odor tuning, leads to their earlier activation than pyramidal cells following odor inhalation. Spike timing only carries information in relation to a reference signal. Our data suggest that fan cells could provide such a reference signal and the synchrony of fan and pyramidal cell firing could be used by downstream areas to read out odor intensity.

Like L2 LEC cells, CA1 neurons preferentially responded early during individual sniffs. Interestingly, firing rates of CA1 cells were completely insensitive to changes in odor concentration. This means that CA1 discards any firing rate changes encoding odor intensity relayed by LEC. Rather, odor intensity was encoded purely by concentration-dependent shifts in spike timing resulting in higher levels of spike synchrony as concentration increased. Temporal coding is thought to contribute to a variety of hippocampal features such as episodic memory and spatial navigation (Dragoi, 2020; Eichenbaum, 2014). The temporal coding of odor intensity in hippocampus is likely also critical for basic behaviors requiring navigation to odor sources.

References

Ache, B.W., Hein, A.M., Bobkov, Y. V., and Principe, J.C. (2016). Smelling Time: A Neural Basis for Olfactory Scene Analysis. Trends Neurosci. *39*, 649–655.

Amaral, D.G., and Witter, M.P. (1989). The three-dimensional organization of the hippocampal formation: A review of anatomical data. Neuroscience *31*, 571–591.

Bathellier, B., Buhl, D.L., Accolla, R., and Carleton, A. (2008). Dynamic ensemble odor coding in the mammalian olfactory bulb: sensory information at different timescales. Neuron *57*, 586–598.

Blazing, R.M., and Franks, K.M. (2020). Odor coding in piriform cortex: mechanistic insights into distributed coding. Curr. Opin. Neurobiol. *64*, 96–102.

Bolding, K.A., and Franks, K.M. (2017). Complementary codes for odor identity and intensity in olfactory cortex. Elife *6*.

Bolding, K.A., and Franks, K.M. (2018). Recurrent cortical circuits implement concentration-invariant odor coding. Science (80-.). *361*.

Bolding, K.A., Nagappan, S., Han, B.X., Wang, F., and Franks, K.M. (2020). Recurrent circuitry is required to stabilize piriform cortex odor representations across brain states. Elife *9*, 1–23.

Boyd, A.M.A.M., Sturgill, J.F.J.F., Poo, C., and Isaacson, J.S.J.S. (2012). Cortical feedback control of olfactory bulb circuits. Neuron *76*, 1161–1174.

Cang, J., and Isaacson, J.S.J.S. (2003). In vivo whole-cell recording of odor-evoked synaptic transmission in the rat olfactory bulb. J. Neurosci. *23*, 4108–4116.

Canto, C.B., and Witter, M.P. (2012). Cellular properties of principal neurons in the rat entorhinal cortex. I. The lateral entorhinal cortex. Hippocampus *22*, 1256–1276.

Chapuis, J., Cohen, Y., He, X., Zhang, Z., Jin, S., Xu, F., and Wilson, D.A. (2013). Lateral entorhinal modulation of piriform cortical activity and fine odor discrimination. J. Neurosci. *33*, 13449–13459.

Chong, E., and Rinberg, D. (2018). Behavioral readout of spatio-temporal codes in olfaction. Curr. Opin. Neurobiol. *52*, 18–24.

Chong, E., Moroni, M., Wilson, C., Shoham, S., Panzeri, S., and Rinberg, D. (2020). Manipulating synthetic optogenetic odors reveals the coding logic of olfactory perception. Science (80-.). *368*.

Cury, K.M., and Uchida, N. (2010). Robust Odor Coding via Inhalation-Coupled Transient Activity in the Mammalian Olfactory Bulb. Neuron *68*, 570–585.

Dragoi, G. (2020). Cell assemblies, sequences and temporal coding in the hippocampus. Curr. Opin. Neurobiol. *64*, 111–118.

Eichenbaum, H. (2014). Time cells in the hippocampus: a new dimension for mapping memories. Nat. Rev. Neurosci. 2014 1511 *15*, 732–744.

Gill, J. V., Lerman, G.M., Zhao, H., Stetler, B.J., Rinberg, D., and Shoham, S. (2020). Precise Holographic Manipulation of Olfactory Circuits Reveals Coding Features Determining Perceptual Detection. Neuron *108*, 382-393.e5.

Haberly, L.B., and Price, J.L. (1978). Association and commissural fiber systems of the olfactory cortex of the rat. II. Systems originating in the olfactory peduncle. J Comp Neurol *181*, 781–807.

Haddad, R., Lanjuin, A., Madisen, L., Zeng, H., Murthy, V.N., and Uchida, N. (2013). Olfactory cortical neurons read out a relative time code in the olfactory bulb. Nat. Neurosci. *16*, 949–957.

Isaacson, J.S., and Scanziani, M. (2011). How inhibition shapes cortical activity. Neuron *72*, 231–243.

Kerr, K.M., Agster, K.L., Furtak, S.C., and Burwell, R.D. (2007). Functional neuroanatomy of the parahippocampal region: The lateral and medial entorhinal areas. Hippocampus *17*, 697–708.

Kitamura, T., Pignatelli, M., Suh, J., Kohara, K., Yoshiki, A., Abe, K., and Tonegawa, S. (2014). Island Cells Control Temporal Association Memory. Science (80-.). *343*, 896–901.

Kobro-Flatmoen, A., and Witter, M.P. (2019). Neuronal chemo-architecture of the entorhinal cortex: A comparative review. Eur. J. Neurosci. *50*, 3627–3662.

Leitner, F.C., Melzer, S., Lütcke, H., Pinna, R., Seeburg, P.H., Helmchen, F., and Monyer, H. (2016). Spatially segregated feedforward and feedback neurons support differential odor processing in the lateral entorhinal cortex. Nat. Neurosci. *19*, 935–944.

Li, Y., Xu, J., Liu, Y., Zhu, J., Liu, N., Zeng, W., Huang, N., Rasch, M.J., Jiang, H., Gu, X., et al. (2017). A distinct entorhinal cortex to hippocampal CA1 direct circuit for olfactory associative learning. Nat. Neurosci. 2017 204 *20*, 559–570.

Lima, S.Q., Hromadka, T., Znamenskiy, P., and Zador, A.M. (2009). PINP: a new method of tagging neuronal populations for identification during in vivo electrophysiological recording. PLoS One *4*, e6099.

Margrie, T.W., and Schaefer, A.T. (2003). Theta oscillation coupled spike latencies yield computational vigour in a mammalian sensory system. J Physiol *546*, 363–374.

Marin, A.C., Schaefer, A.T., and Ackels, T. (2021). Spatial information from the odour environment in mammalian olfaction. Cell Tissue Res. *383*, 473–483.

Masurkar, A. V., Srinivas, K. V., Brann, D.H., Warren, R., Lowes, D.C., and Siegelbaum, S.A. (2017). Medial and Lateral Entorhinal Cortex Differentially Excite Deep versus Superficial CA1 Pyramidal Neurons. Cell Rep. *18*, 148–160.

Nilssen, E.S., Jacobsen, B., Fjeld, G., Nair, R.R., Blankvoort, S., Kentros, C., and Witter, M.P. (2018). Inhibitory connectivity dominates the fan cell network in layer ii of lateral entorhinal cortex. J. Neurosci. *38*, 9712–9727.

Petreanu, L., Mao, T., Sternson, S.M., and Svoboda, K. (2009). The subcellular organization of neocortical excitatory connections. Nature *457*, 1142–1145.

Poo, C., and Isaacson, J.S.J.S. (2009). Odor representations in olfactory cortex: "sparse" coding, global inhibition, and oscillations. Neuron *62*, 850–861.

Radvansky, B.A., and Dombeck, D.A. (2018). An olfactory virtual reality system for mice. Nat. Commun. 2018 91 *9*, 1–14.

Schaffer, E.S., Stettler, D.D., Kato, D., Choi, G.B., Axel, R., and Abbott, L.F. (2018). Odor Perception on the Two Sides of the Brain: Consistency Despite Randomness. Neuron *98*, 736-742.e3.

Schoonover, C.E., Ohashi, S.N., Axel, R., and Fink, A.J.P. (2021). Representational drift in primary olfactory cortex. Nature *594*.

Shusterman, R., Smear, M.C., Koulakov, A.A., and Rinberg, D. (2011). Precise olfactory responses tile the sniff cycle. Nat. Neurosci. *14*, 1039–1044.

Sirotin, Y.B., Shusterman, R., and Rinberg, D. (2015). Neural coding of perceived odor intensity. ENeuro *2*.

Sosulski, D.L., Lissitsyna Bloom, M., Cutforth, T., Axel, R., and Datta, S.R. (2011). Distinct representations of olfactory information in different cortical centres. Nature *472*, 213–219.

Stern, M., Bolding, K.A., Abbott, L.F., and Franks, K.M. (2018). A transformation from temporal to ensemble coding in a model of piriform cortex. Elife *7*.

Stettler, D.D., and Axel, R. (2009). Representations of odor in the piriform cortex. Neuron *63*, 854–864.

Tahvildari, B., and Alonso, A. (2005). Morphological and electrophysiological properties of lateral entorhinal cortex layers II and III principal neurons. J. Comp. Neurol. *491*, 123–140.

Uchida, N., and Mainen, Z.F. (2003). Speed and accuracy of olfactory discrimination in the rat. Nat Neurosci *6*, 1224–1229.

Uchida, N., Poo, C., and Haddad, R. (2014). Coding and transformations in the olfactory system. Annu. Rev. Neurosci. *37*, 363–385.

Vandrey, B., Garden, D.L.F., Ambrozova, V., McClure, C., Nolan, M.F., and Ainge, J.A. (2020). Fan Cells in Layer 2 of the Lateral Entorhinal Cortex Are Critical for Episodic-like Memory. Curr. Biol. *30*, 169-175.e5.

Wilson, D.A., and Sullivan, R.M. (2011). Cortical processing of odor objects. Neuron *72*, 506–519.

Wilson, R.I., and Mainen, Z.F. (2006). Early events in olfactory processing. Annu Rev Neurosci

29, 163–201.

Wilson, C.D., Serrano, G.O., Koulakov, A.A., and Rinberg, D. (2017). A primacy code for odor identity. Nat. Commun. *8*.

Woods, N.I., Stefanini, F., Apodaca-Montano, D.L., Tan, I.M.C., Biane, J.S., and Kheirbek, M.A. (2020). The Dentate Gyrus Classifies Cortical Representations of Learned Stimuli. Neuron *107*, 173-184.e6.

Xu, W., and Wilson, D.A. (2012). Odor-evoked activity in the mouse lateral entorhinal cortex. Neuroscience *223*, 12–20.

Methods

All animal procedures were in accordance with protocols approved by the University of California, San Diego Institutional Animal Care and Use Committee and guidelines of the National Institutes of Health. Both female and male mice (>6 weeks old) were used for *in vivo* experiments. The following strains were obtained from JAX (stock number): C57BL/6J (000664), Tbet-cre (024507), GAD2-Cre (010802), PV-cre (008069), SOM-cre (013044), Calbindin-cre (028532), Ai14(RCL-tdT) (007914), and Ai32(RCL-ChR2(H134R)/EYFP) (024109). Ntsr1-cre mice (Tg(Ntsr1-cre)209Gsat) were obtained from the Gensat Project. Cre^+ neurons in olfactory cortical areas have previously been characterized as pyramidal neurons (Boyd et al., 2012; Stokes and Isaacson, 2010). NetrinG1-cre mice were kindly provided by Fan Wang (Duke University). Mice were maintained on a 12:12 reversed light:dark cycle and experiments were performed during the dark period.

Viral and retrobead injections

NetrinG1-cre x Ai14 mice or Calbindin-cre x Ai14 were anesthetized (2% isoflurane) and injected with AAV1-CAG-FLEX-tdTomato (200 nl at 20 nl/min, Addgene #28306) into the LEC (coordinates: ~3.6 mm posterior to bregma, 1.5-2.0 mm ventral to the lateral ridge on the posterior part of the temporal bone, 0.3-0.4 mm from dura at a 90º angle). Orientation of the LEC was assisted by visualizing the rhinal vein through the skull. For bead injections, Ntsr1-cre x Ai14, NetrinG1-cre x Ai14 mice, or Calbindin-cre x Ai14 were anesthetized (2% isoflurane) and injected with green RetroBeads (500 nl at 100 nl/min, Lumafluor) into the DG (coordinates from bregma: 3.0 mm posterior, 2.0 mm lateral, 2.5 mm ventral from dura) or the OB (coordinates from bregma: 5.0 mm anterior, 0.8 mm lateral, 0.5 mm ventral from dura), respectively. After all injections, mice

received dexamethasone (2 mg/kg) and buprenorphine (0.1 mg/kg) before return to their home cage. Mice were used for experiments four weeks after viral injections and three days after bead injections.

For *in vitro* recordings of PCx input to LEC, neonatal mice (postnatal day 0-2) were anesthetized by hypothermia and AAV9-hSyn-hChR2(H134R)-eYFP-WPRE-hGH was injected at four sites (23 nl/site, depths of 0.18-0.25 mm) targeting the anterior PCx based on landmarks including the superficial temporal vein and the posterior border of the eye (Boyd et al., 2012). Brain slices were made 3-4 weeks after injection.

Immunohistochemistry

Mice used for histology were transcardially perfused with 4% paraformaldehyde in PBS and the brains extracted. Fixed brains were kept in 4% paraformaldehyde at 4°C for 24 h and in 30% sucrose for 24-48 h. Coronal sections were cut at 50 μm. Free floating sections were washed in TBS, permeabilized and blocked in TBS containing 10% horse serum and 0.2% Triton-X-100, and incubated overnight with primary antibodies (mouse anti-reelin, 1:2000, MAB5364, Merck Millipore; rabbit anti-calbindin, 1:5000, CB-38a, Swant). Slices were washed in TBS, incubated for 2 h with secondary antibodies (goat anti-mouse Alexa Fluor 488, 1:500, A11029, Thermo Fisher; goat anti-rabbit Alexa Fluor 488, 1:500, A11008, Thermo Fisher; goat anti-rabbit Alexa Fluor 647, 1:500, A32733, Thermo Fisher). Slices were mounted on slides (Vectashield medium with DAPI), imaged using a confocal microscope (Leica SP8) and subsequently analyzed with ImageJ.

Brain slice experiments

Mice were anesthetized with isoflurane and decapitated. Brains were removed and placed into ice-cold artificial cerebrospinal fluid (aCSF) containing (in mM) 83 NaCl, 2.5 KCl2, 0.5 CaCl2, 3.3 MgSO4, 1 NaH2PO4, 26.2 NaHCO3, 22 glucose and 72 sucrose, equilibrated with 95% O2 and 5% CO2. Coronal slices (300–400 μm thickness) containing the LEC were cut using a vibrating slicer and incubated at 35 °C for 30 min. Slices were transferred to a recording chamber and superfused with aCSF containing (in mM) 119 NaCl, 5 KCl, 2.5 CaCl2, 1.3 MgSO4, 1 NaH2PO4, 26.2 NaHCO3 and 22 glucose, equilibrated with 95% O2 and 5% CO2. All experiments were conducted at 28–30 °C.

Patch-clamp recordings were performed using an upright microscope and DIC optics. Recordings were made using a Multiclamp 700A amplifier (Molecular Devices) digitized at 20 kHz and acquired using AxographX software. For current clamp recordings, pipettes (3–6 MΩ) contained (in mM) 150 potassium gluconate, 1.5 MgCl2, 5 HEPES buffer, 0.1 EGTA 10 phosphocreatine and 2.0 Mg-ATP, pH 7.4). For voltage clamp recordings, the internal solution contained (in mM): 130 D-gluconic acid, 130 CsOH, 5 NaCl, 10 HEPES, 0.2 EGTA, 12 phosphocreatine, 3 Mg-ATP, and 0.2 Na-GTP [pH 7.3]). Biocytin (0.2%) was added to the pipette to allow for recovery of cell morphology. Series resistance was routinely <20 MΩ and continuously monitored. Output from a collimated LED light source (470 nm, ThorLabs) was directed through the 40× microscope objective for full-field photoactivation of ChR2.

For reconstruction of biocytin-filled cells, slices were fixed overnight in 4% PFA and then transferred into 30% sucrose. Biocytin was immunolabeled using 1:500 Alexa Fluor 488 strepavidin (Invitrogen, S32354). Slices were mounted on slides (Vectashield), imaged using a two-photon microscope (Olympus Fluoview) and subsequently analyzed with ImageJ.

Olfactory driven behavior

Under isoflurane anesthesia (2%), GAD2-cre x Ai32 or GAD2-cre mice were implanted with a metal head bar for head fixation. The skull above the LEC was exposed bilaterally by carefully detaching muscles from the lateral ridge of the skull which was covered with a thin layer of transparent cyanoacrylate glue to create a window for LED illumination. After implantation, mice received dexamethasone (2 mg/kg) and buprenorphine (0.1 mg/kg) before returning to their home cage. Behavioral experiments were conducted using Bpod State Machines (Sanworks). After >7 days of recovery, mice were water deprived (1 ml/day) and accustomed to handling and head fixation. Subsequently, mice were trained to lick for water in response to odor stimulation and trained to discriminate odor identity (isoamyl acetate 1% v/v vs. limonene 1% v/v in mineral oil) or odor intensity (ethyl tiglate 0.25% vs. 1% v/v in mineral oil) for several days in a 2AFC task until they reached the criterion of 75% correct choices. Mice indicated their choices by licking one of two lick ports for a water reward (5 μl). Respiration was recorded with a pressure sensor at the nose. Trials were initiated with a 50 ms tone. A custom-made closed-loop olfactometer was used for precisely timed and stable odor stimulation triggered by respiration. Odors were delivered for 1 s and mice were given a 2 s response time from the start of odor delivery. Error trials were followed by a 4 s timeout. On test day, mice performed the 2-AFC task with bilateral optogenetic silencing of the LEC (transcranial stimulation with fiber-coupled LEDs, Thorlabs, 470 nm, 1000 μm core fibers, 10 ms pulses, 20 Hz) randomly on 25% of trials. LED fibers were shielded to minimize light leakage. Control experiments were performed using GAD2-cre x Ai32 mice in which the optical windows above LEC was shielded from LED illumination or GAD2-cre mice that were not expressing ChR2. For analysis of response times, all trials were aligned to the onset of the first inhalation after stimulus onset.

In vivo recordings and olfactory stimulation

Mice were implanted with a metal head bar for head fixation as described previously. The skull above the OB (coordinates from bregma: 5.0 mm anterior, 0.8 mm lateral), PCx (coordinates from bregma: 1.7 mm anterior, 2.5 mm lateral), LEC (see above and Supplemental Fig. 1B), and/or CA1 (coordinates from bregma: 3.6 mm posterior, 4.4 mm lateral) was exposed and electrode insertion sites were marked on the skull. After >4 days of recovery, mice were accustomed to handling and head fixation. During recording, awake mice sat quietly in a loosely fitted plastic tube. Silicon probes were inserted into the OB (16-channel, Neuronexus, 0.5 mm from dura), PCx (32-channel, Cambridge Neurotech, 3.6 mm from dura), LEC (32-channel, Cambridge Neurotech, 0.8 mm from dura at a 90º angle), and/or CA1 (64-channel, Cambridge Neurotech, 2.2 mm from dura at a 45º angle). Electrodes were left in place for ~45 min before recordings were initiated. Signals were recorded using an Open Ephys acquisition board and digitized at 20 kHz using Open Ephys software. Probes were coated in DiI to verify recording locations post-hoc.

A custom-made, Arduino-controlled closed-loop olfactometer was used for precisely timed and stable odor stimulation triggered by respiration. Odor timing was verified using a fast PID (Aurora Scientific). For odor trials, charcoal-filtered air (1 l/min) was directed to glass vials containing monomolecular odorants (Fig. 3, 1% v/v in mineral oil) or an odor blank (mineral oil alone) using mass flow controllers. Odors were delivered in randomized order and concentrations of 0.25, 0.33, 0.50, and 1% were achieved by adding 0 to 3 blank lines to the odor line. Recordings were made using 25 repetitions of each odor at each concentration.

For phototagging of cells in NetrinG1-cre x Ai32 and Calbindin-cre x Ai32 mice, a fiber-coupled LED (470 nm, 400 μm core fiber, Thorlabs) was positioned within 1 mm of the exposed

skull above the LEC. 5 ms light pulses were used to excite ChR2-expressing NetrinG1-cre or Calbindin-cre neurons. Tagged units were identified based on a significant increase in firing rate and consistent spike latency within a 5 ms window from LED onset (Kvitsiani et al., 2013). For recordings of responses to ChR2 activation of OB mitral cells in Tbet-cre x Ai32 mice, the fiber-coupled LED was positioned within 1 mm of the exposed skull above the OB.

In vivo data analysis

Analysis was performed using MATLAB R2018b (MathWorks). Spikes were sorted using Kilosort2 (https://github.com/MouseLand/Kilosort), followed by manual curation in Phy (https://github.com/cortex-lab/phy) to obtain single units used for analyses. Cells were excluded from analysis if they did not maintain consistent firing and amplitude throughout the recording. For analysis of odor-evoked activity, all stimulation trials were aligned to the onset of the first inhalation of odor. Units were considered activated when mean firing rate in response to odor stimulation significantly increased compared to blank stimulation using paired t-tests ($p<0.05$). Spike-density functions were calculated using a gaussian kernel (σ=10 ms) and averaged across trials. Lifetime sparseness of single units was calculated based on the mean firing rate change across odors as:

$\left(1-\left(\left(\sum_{j=1,N} r_j/N\right)^2/\left(\sum_{j=1,N} r_j^2/N\right)\right)\right)/(1-1/N)$, where r_j is the response of the unit to odor j and N is the total number of odors. Negative responses were set to 0 for this measure. This provides a measure of how selective the response of a unit was distributed among all odors (completely selective = 1, non-selective = 0).

Principal component analysis was performed on pseudopopulation responses of all recorded units. Euclidean distance was computed on the first three principal components in 1 ms bins. Support vector machine classification was performed on pseudopopulation responses of all recorded units in a one-vs-one coding scheme with 20% holdout validation to test the model. Statistical comparisons were performed using paired and unpaired t-tests, and spearman's rank correlations.

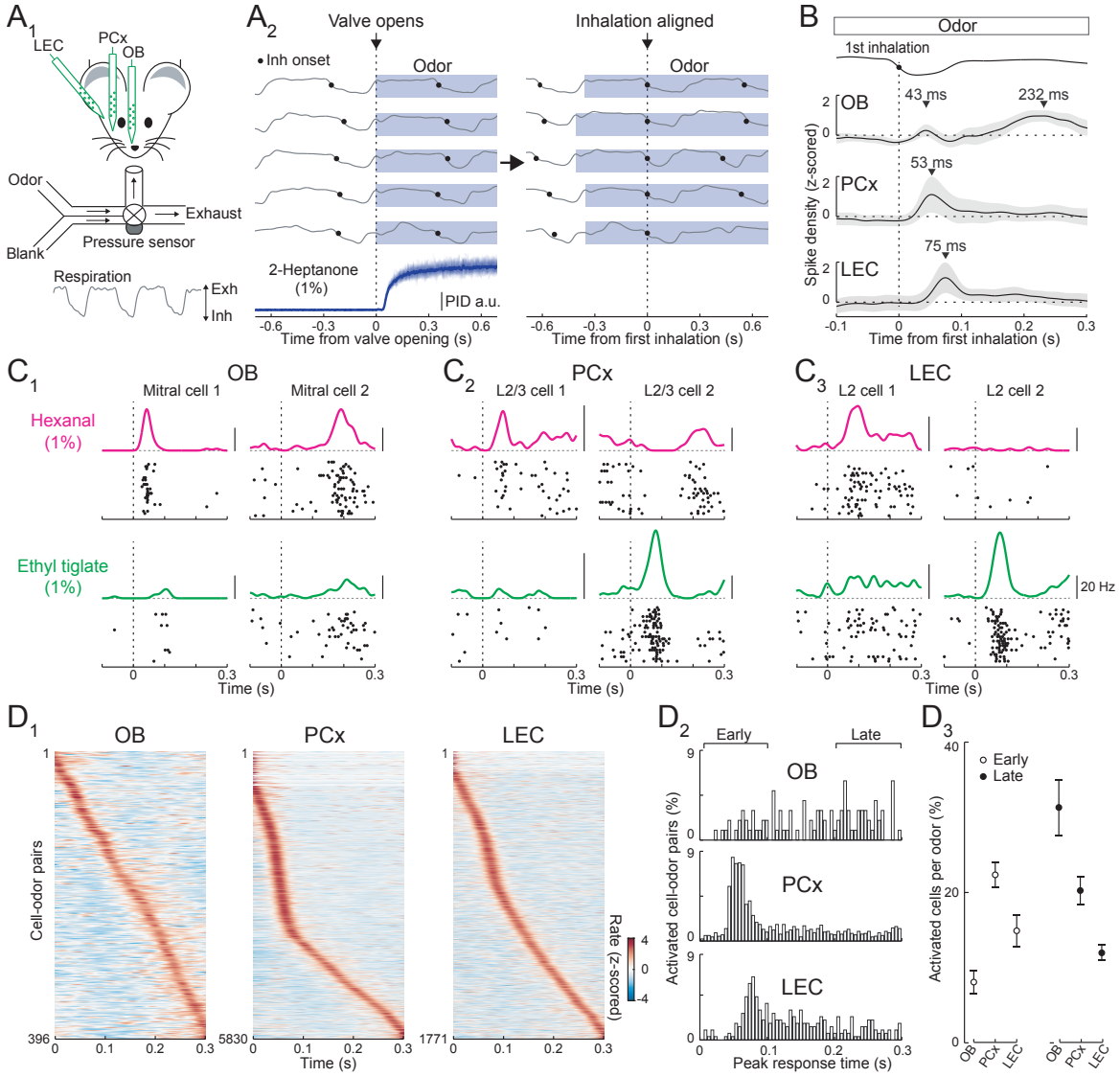

Figure 1: Rapid responses dominate odor-evoked activity in LEC L2.

(**A**) System for recording of odor-evoked activity aligned to onset of first inhalation of odor. (**A$_1$**) Experimental setup for triple recordings of odor-evoked activity in the OB, anterior PCx, and LEC of awake head-fixed mice. Downward and upward deflections on respiration trace from pressure sensor indicate inhalation (Inh) and exhalation (Exh), respectively. (**A$_2$**) Left, respiration signals during odor delivery (blue shading) for five trials are plotted above PID measurement of odor (2-Heptanone) at the sampling port. Black circles, inhalation onset. Right, same respiration signals aligned to onset of first inhalation. (**B**) OB mitral cell odor responses during individual sniffs have both early and late components, while early responses dominate in PCx and LEC. Spike density plots of single unit activity averaged across all triple recordings (n=6 mice) from OB (n=36 cells), PCx (n=530 cells), and LEC (n=161 cells) responses to 11 odors. Trials were aligned to the first inhalation during each odor (dashed line). Top trace, representative averaged respiration trace from one experiment. (**C**) Raster plots and spike-density functions of odor-evoked activity for two representative cells from OB (**C$_1$**), PCx (**C$_2$**), and LEC (**C$_3$**) in response to hexanal (top) and ethyl tiglate (bottom). (**D**) OB mitral cell responses occur evenly across the entire respiration cycle, while responses of PCx L2/3 cells and LEC L2 cells often occur early following odor inhalation. (**D$_1$**) Plots of odor-evoked firing rates for all cell-odor pairs rank ordered by time of peak firing for OB mitral cells (left), PCx L2/3 cells (middle) and LEC L2 cells (right). (**D$_2$**) Histograms showing time of peak odor responses relative to inhalation onset for significantly activated cell-odor pairs in the OB, PCx, and LEC. (**D$_3$**) Percent of activated cells per odor in the OB, PCx, and LEC during the early (0-100 ms) and late (200-300 ms) phase of odor-evoked activity marked in **D$_2$**. Error bars represent SEM.

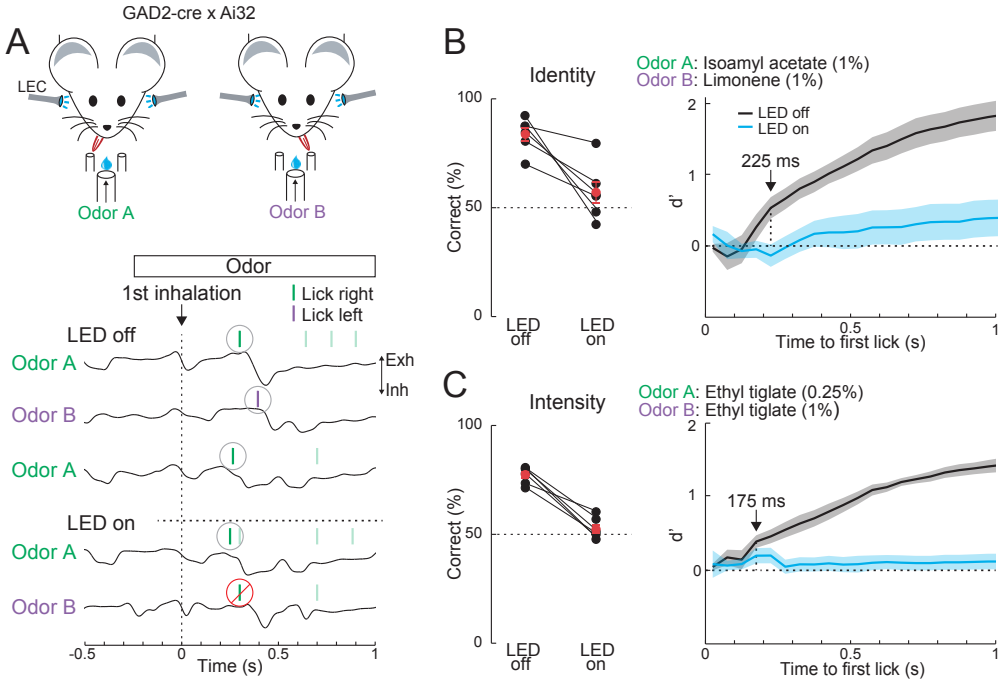

Figure 2: LEC is essential for rapid odor-driven behavior.

(**A**) Top, experimental setup for 2AFC odor-driven behavior with bilateral optogenetic silencing of the LEC in head-fixed mice expressing ChR2 in GABAergic neurons. Bottom, representative respiration traces aligned to the first inhalation of odor and superimposed lick responses (colored bars) during odor discrimination. (**B**) LEC is required for discrimination of odor identity. Left, percent of correct choices for mice trained to discriminate different odors (isoamyl acetate vs. limonene, both at 1.0%) on trials with (LED on) and without (LED off) optogenetic LEC silencing (n=6 mice). Right: d' of cumulative responses over time. Under control conditions (LED off), d' becomes significantly different 225 ms following odor inhalation. (**C**) LEC is required for discrimination of odor intensity. Left, percent of correct choices for mice trained to discriminate different concentrations of the same odor (0.25% vs. 1.0% ethyl tiglate) for trials with and without LEC silencing (n=6 mice). Right: d' of cumulative responses over time. Under control conditions (LED off), d' becomes significantly different 175 ms following odor inhalation. Error bars represent SEM.

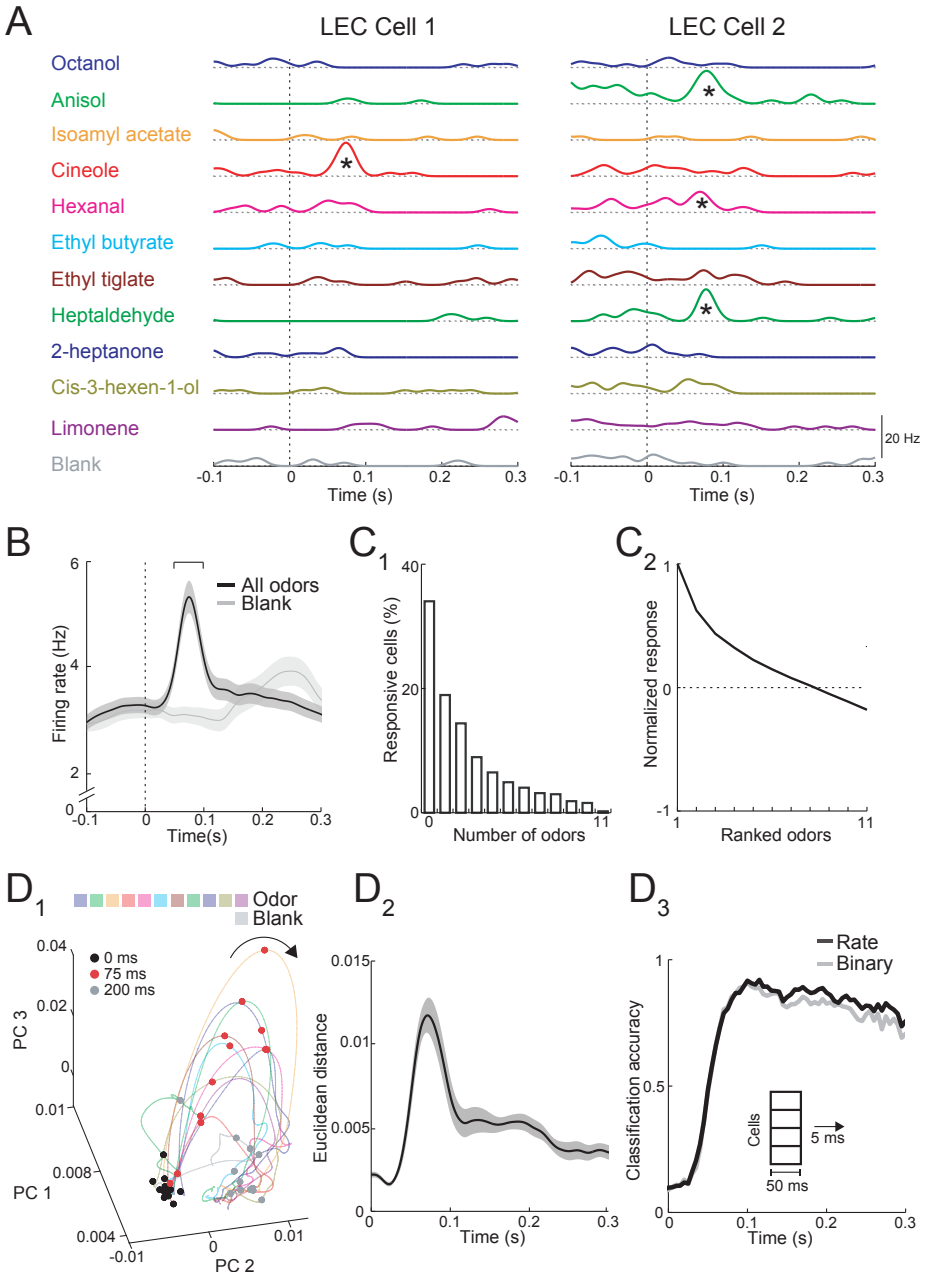

Figure 3: Rapid increases in firing rate encode odor identity in LEC L2.

(**A**) Spike density functions of inhalation-aligned odor evoked activity (11 odors and blank) for two representative LEC L2 cells. Asterisks, significant odor-evoked increases in firing rate. (**B**) Averaged spike density function of activity in LEC L2 (n= 576 cells, 11 odors, 19 recordings) shows early increase in firing rate for odor-evoked responses (black line) vs. baseline respiration-coupled activity (blank, grey line). Bracket, 50 ms window used to measure early odor-evoked firing. (**C**) Odor identity is encoded by overlapping ensembles of active cells. (**C_1**) Percent of cells responsive from 0 to 11 odors. (**C_2**) Normalized and ranked odor-evoked firing rate change relative to blank in LEC L2. (**D**) Principal component analysis reveals that LEC cell ensembles can rapidly distinguish odor identity. (**D_1**) Trajectories of the first three principal components of odor-evoked activity in LEC L2 over time following odor inhalation (each odor indicated by different colored line). Circles represent time points relative to odor inhalation: 0 ms (black), 75 ms (red) and 200 ms (grey). (**D_2**) Euclidean distance of the first three principal components between 11 odors (binned over 1 ms time window) shows discriminability peak within 100 ms of odor inhalation. (**D_3**) A linear classifier can rapidly discriminate odor identity from early odor-evoked changes in firing rate or binary categorization of activity. Classification accuracy is plotted using mean firing rate (black) or binary measure of cell activation (grey) using a 50 ms sliding window with 5 ms steps. Error bars represent SEM.

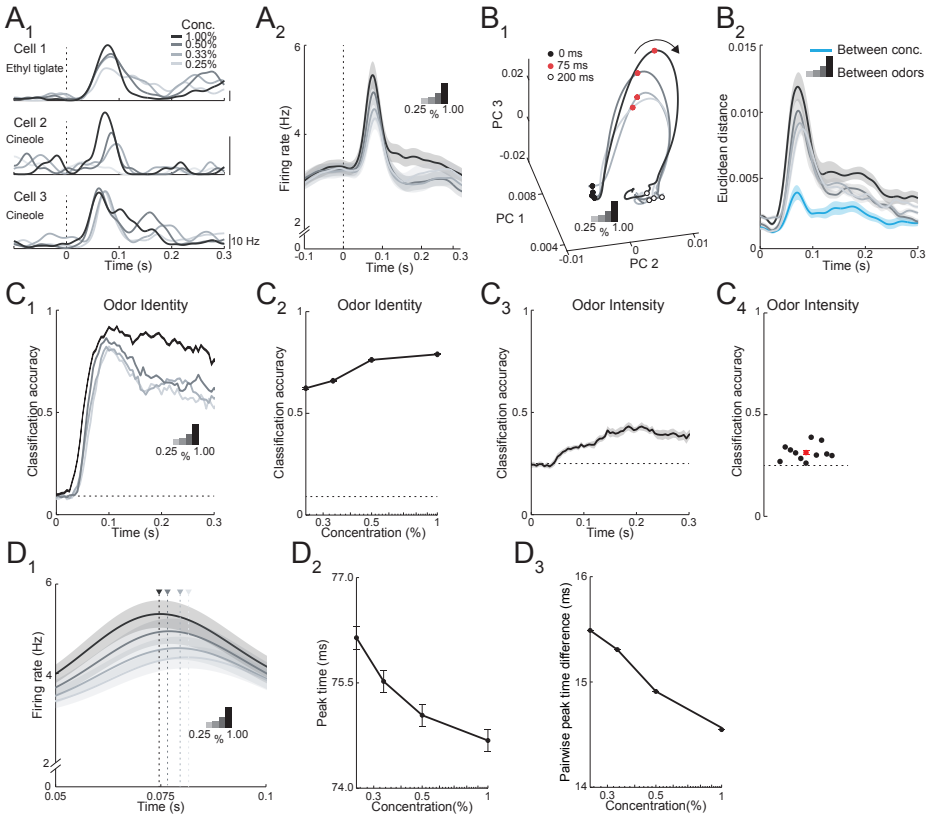

Figure 4: Both rate and timing of odor-evoked activity encode odor intensity in LEC L2. (**A**) Changes in odor concentration alter firing rates and spike timing in LEC. (**A$_1$**) Spike density functions of odor evoked activity for three representative LEC L2 cell-odor pairs at four concentrations indicated by line shading (0.25, 0.33, 0.50, and 1.00%). (**A$_2$**) Averaged spike density function of odor-evoked activity aligned to the first inhalation across four concentrations of the same odors for the LEC L2 cell population (n=576 cells, 11 odors at 0.25, 0.33, 0.50, 1.00%, 19 recordings). (**B**) Principal component analysis of the cell population for responses to four odor concentrations indicates that firing rate can be used to discriminate odor intensity, but discriminability is poorer than that for odor identity. (**B$_1$**) Trajectories of the first three principal components of odor-evoked activity over time following odor inhalation (each odor concentration indicated by a different line shading). Circles represent time points relative to odor inhalation: 0 ms (filled black), 75 ms (red) and 200 ms (open black). (**B$_2$**) Euclidean distance of the first three principal components of odor evoked activity in the LEC between responses of the four concentrations (blue) shows a peak in discriminability within 100 ms of odor inhalation. The discriminability between responses of the same cells to 11 odors for the four different intensities (gray to black) is much higher. Responses are binned with a 1 ms time window. (**C**) A linear classifier shows that odor identity discrimination somewhat improves as odor concentration increases and that odor intensity can be weakly discerned from firing rate changes. (**C$_1$**) Classification accuracy for odor identity at the four concentrations indicated by the shaded lines using a 50 ms sliding window with 5 ms steps. (**C$_2$**) Classification accuracy of odor identity at different concentrations based on average firing rate in a fixed window 50-100 ms following odor inhalation. (**C$_3$**) Classification accuracy of odor intensity for each odor based on average firing rate using a sliding window. (**C$_4$**) Classification accuracy of odor intensity for each odor based on average firing rate in a fixed window 50-100 ms following odor inhalation. (**D**) Spike timing effectively encodes odor intensity. (**D$_1$**) Blow-up of data from (A$_2$) shows shift in timing of peak responses with odor concentration. Arrowheads mark peak times at the four concentrations. (**D$_2$**) Peak time of odor-evoked activity averaged across all cell-odor pairs shifts with changes in odor concentration. (**D$_3$**) Mean pairwise peak time difference of odor-evoked activity for cell-odor pairs indicates that spike firing becomes more synchronized as odor concentration increases. Error bars represent SEM

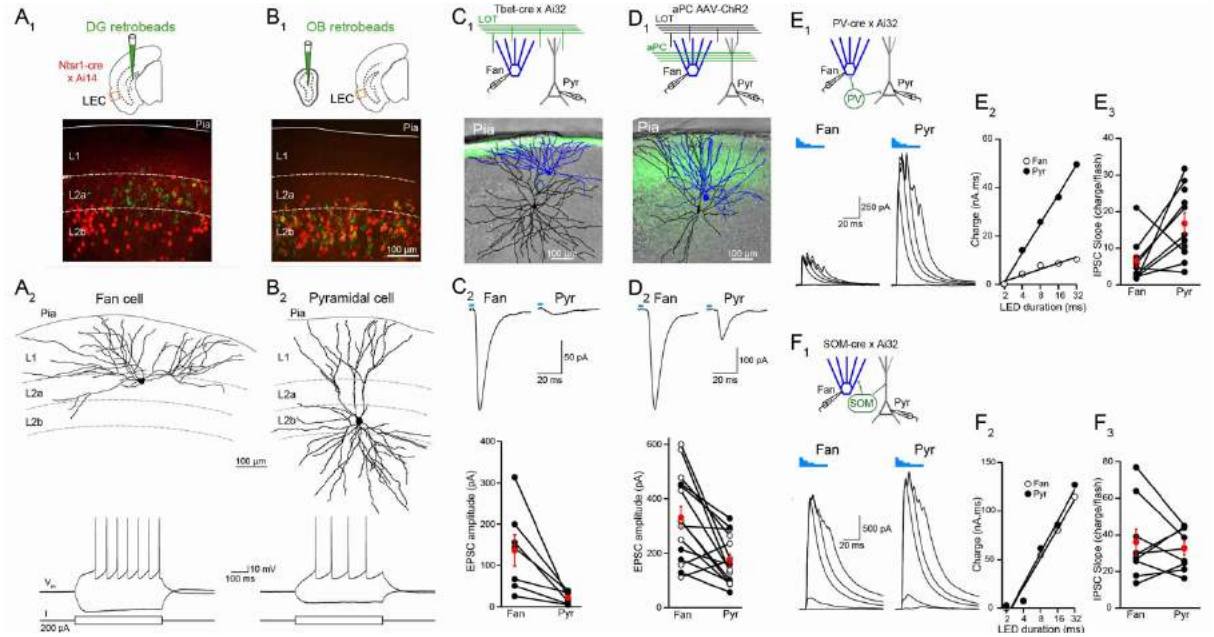

Figure 5: L2 fan and pyramidal cells differ in olfactory input and inhibitory circuit connectivity.

(**A**) Anatomical and intrinsic electrophysiological properties of fan cells. (**A_1**) Top, schematic of retrobead injection into the DG of Ntsr1(209)-cre mice expressing TdTomato. Bottom, image of LEC region outlined in schematic showing DG-projecting cells (green) located in L2a and Ntsr1-positive cells (red) concentrated in L2b. (**A_2**) Targeted brain slice recording from a DG-projecting fan cell. Top, post-hoc reconstruction of fan cell dendritic arbor. Bottom, membrane potential response to depolarizing and hyperpolarizing current steps. (**B**) Anatomical and intrinsic electrophysiological properties of pyramidal cells. (**B_1**) Top: schematic of retrobead injection into the OB of Ntsr1(209)-cre mice expressing TdTomato. Bottom, image of LEC region outlined in schematic showing OB-projecting cells (green) and Ntsr1-positive cells (red) co-localize in L2b. (**B_2**) Targeted brain slice recording from an OB-projecting pyramidal cell. Top, post-hoc reconstruction of pyramidal cell dendritic arbor. Bottom, membrane potential response to depolarizing and hyperpolarizing current steps. (**C**) Fan cells receive stronger direct olfactory bulb input than pyramidal cells. (**C_1**) Top, recording schematic for paired recordings of fan and pyramidal cells in LEC slices expressing ChR2 in LOT fibers. Bottom, post-hoc reconstruction of simultaneously recorded fan cell (blue) and pyramidal cell (black) overlaid on image of LEC slice showing ChR2 expression in LOT (green). (**C_2**) Top, LED-evoked EPSCs in simultaneously recorded fan and pyramidal cells from C_1. Blue bar, LED flash. Bottom, summary of EPSC amplitudes elicited by stimulation of OB input. Black circles, individual cells. Red circles, mean ± SEM. (**D**) Fan cells receive stronger direct piriform cortex input than pyramidal cells. (**D_1**) Top, recording schematic for paired recordings in LEC slices expressing ChR2 in PCx inputs. Bottom, post-hoc reconstruction of simultaneously recorded fan cell (blue) and pyramidal cell (black) overlaid on image of LEC slice showing ChR2 expression in PCx fibers (green). (**D_2**) Top, LED-evoked EPSCs in simultaneously recorded fan and pyramidal cells from D_1. Blue bar, LED. Bottom, summary of EPSC amplitudes elicited by stimulation of PCx input. Black circles, individual cells in control aCSF. Open circles, cells recorded in the presence of tetrodotoxin (1 μM) and 4-aminopyridine (100 μM). Red circles, mean ± SEM. (**E**) Fan cells receive less PV cell-mediated inhibition than pyramidal cells. (**E_1**) Top, recording schematic. Bottom, LED-evoked IPSCs elicited in simultaneously-recorded fan and pyramidal cells. Traces indicate responses to five LED pulses of increasing duration (blue bars). (**E_2**) Inhibitory charge for fan cell (open circles) and pyramidal cell (filled circles) shown in E_1. Lines fit to points are used to measure slope of input-output relationship. (**E_3**) Summary of IPSC slopes for fan and pyramidal cells in response to activation of PV cells. Black circles, individual cells. Red circles, mean ± SEM. (**F**) Fan cells and pyramidal cells receive similar SOM cell-mediated inhibition. (**F_1**) Top, recording schematic. Bottom, LED-evoked IPSCs elicited in simultaneously-recorded fan and pyramidal cells. Traces indicate responses to five LED pulses of increasing duration (blue bars). (**F_2**) Inhibitory charge for fan cell (open circles) and pyramidal cell (filled circles) shown in F_1. (**F_3**) Summary of IPSC slopes for fan and pyramidal cells in response to activation of PV cells. Black circles, individual cells. Red circles, mean ± SEM.

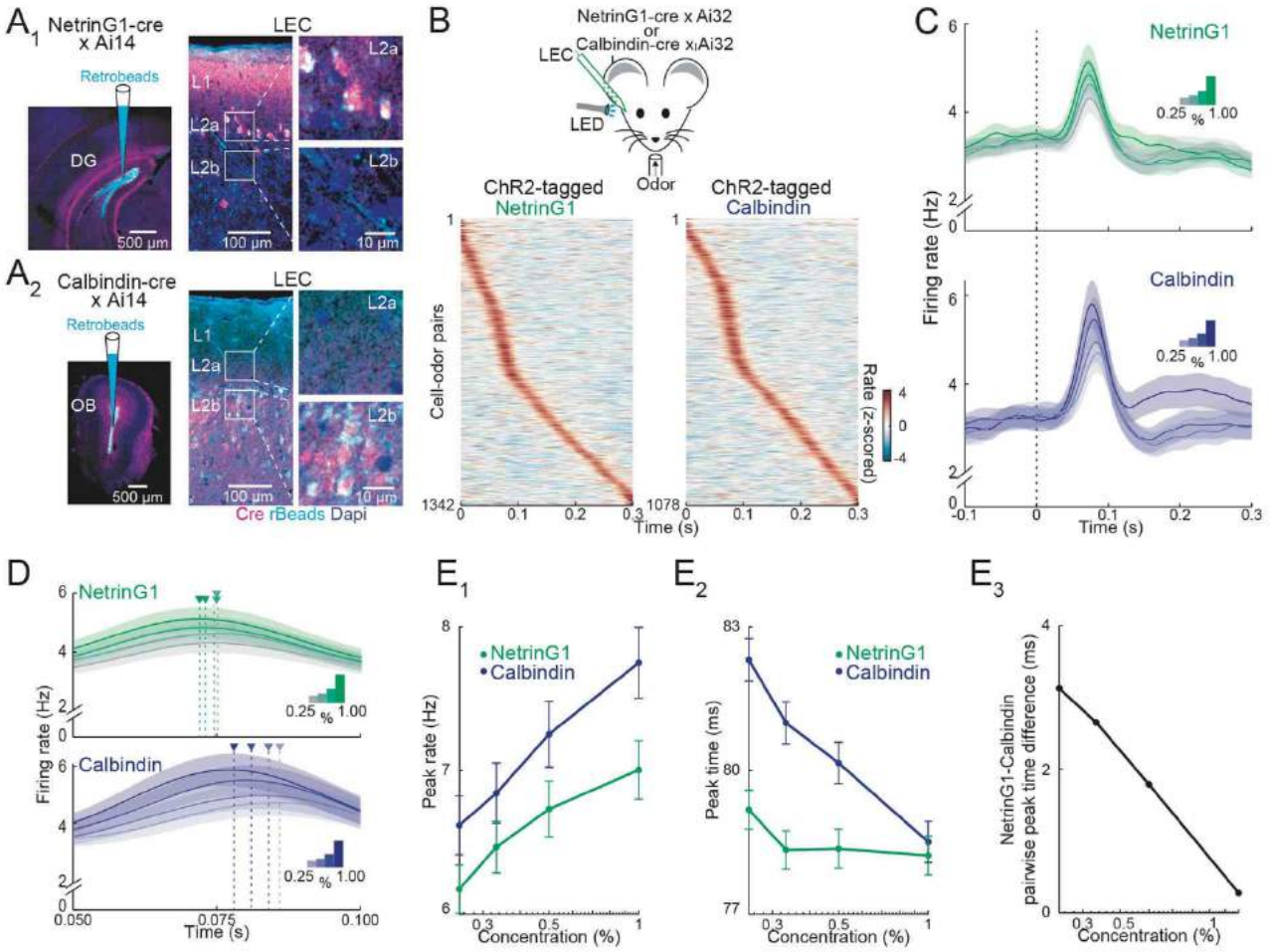

Figure 6: Temporal coding of odor intensity by fan and pyramidal cells

(**A**) Transgenic mouse lines allow targeting of L2 fan and pyramidal cells in LEC. (**A$_1$**) NetrinG1-cre expression in L2a fan cells. Left, Site of DG retrobead (blue) injection in NetrinG1-cre x Ai14 mouse. Right, LEC section indicates cre restricted to DG-projecting cells in L2a. (**A$_2$**) Calbindin-cre expression in L2b pyramidal cells. Left, Site of OB retrobead (blue) injection in Calbindin-cre x Ai14 mouse. Right, LEC section indicates cre within OB-projecting cells in L2b. (**B**) Odors evoke rapid responses in optogenetically-tagged fan and pyramidal cells. Top, experimental setup. Bottom, Plots of odor-evoked firing rates for all cell-odor pairs rank ordered by time of peak firing for ChR2-tagged NetrinG1 (left) and Calbindin (right) neurons (n=122 cells; 12 recordings and 98 cells; 7 recordings, respectively). (**C**) Odor concentration-dependent timing of pyramidal cell activity. Average time course of activity evoked by different odor concentrations (0.25, 0.33, 0.50, 1.00%) for tagged NetrinG1/fan (top) and Calbindin/pyramidal (bottom) cells. (**D**) Traces in (C) shown on a faster timescale. Arrowheads mark times of peak firing for the different intensities. (**E**) Changes in odor concentration shift spike timing of pyramidal cells relative to fan cells. (**E$_1$**) Peak rates of odor-evoked activity at different intensities for NetrinG1/fan and Calbindin/pyramidal cell-odor pairs. (**E$_2$**) Peak times of odor-evoked activity at different intensities reveals strong dependence on odor concentration for Calbindin/pyramidal but not NetrinG1/fan cells. (**E$_3$**) Synchrony between fan and pyramidal cell firing depends on odor concentration. Pairwise peak time differences of NetrinG1/fan and Calbindin/pyramidal cell-odor pairs decrease as odor concentration increases. Error bars represent SEM.

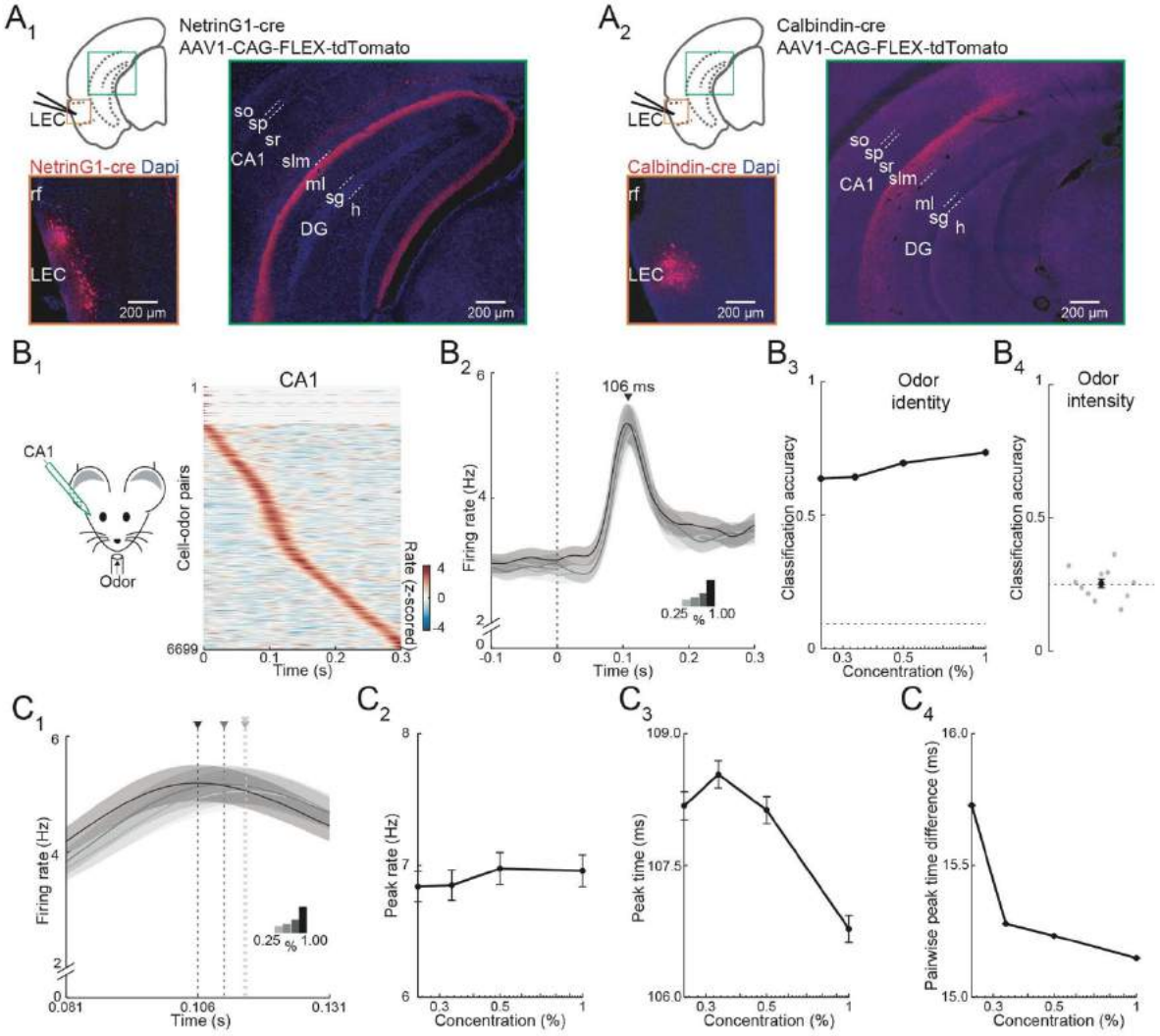

Figure 7: Purely temporal coding of odor intensity in CA1.

(**A**) Fan and pyramidal cells target distinct hippocampal regions. (**A$_1$**) Schematic of fan cell anterograde viral tracing strategy in NetrinG1-cre mice and images showing AAV-FLEX-tdTomato expression (red) at LEC injection site (left) and projections concentrated in DG (right). (**A$_2$**) Schematic of pyramidal cell tracing strategy in Calbindin-cre mice and images showing AAV-FLEX-tdTomato expression (red) at LEC injection site (left) and projections concentrated in CA1 stratum (s.) lacunosum moleculare (slm, right). Hippocampal regions: so, s. oriens; sp, s. pyramidale; sr, s. radiatum; ml, DG molecular layer; sg, DG s. granulosum; h, DG hilus. (**B**) Rapid odor-evoked changes in firing rate encode odor identity but not intensity in CA1 pyramidal cells. (**B$_1$**) CA1 pyramidal cells respond rapidly to odors. Left, experimental setup. Right, odor-evoked firing rates for all cell-odor pairs rank ordered by time of peak firing in CA1 (n=609 cells, 11 odors, 19 recordings).(**B$_2$**) Average activity at four odor concentrations for CA1 cells (n=609 cells, 19 recordings) aligned to inhalation onset show that firing rate is independent of odor concentration. (**B$_3$**) Firing rate encodes odor identity in CA1. Plot shows classification accuracy of odor identity at the different intensities (0.25, 0.33, 0.50, 1.00%) based on the average firing rate in a fixed time window (81-131 ms after inhalation onset). Chance, dotted line. (**B$_4$**) Firing rate does not encode odor intensity. Classification accuracy of odor intensity for 11 odors based on average firing rate in the same fixed time is no better than chance (dotted line). (**C**) Odor intensity encoded by spike timing changes in CA1. (**C$_1$**) Data from (B$_2$) on a faster timescale shows odor concentration-dependent shift in timing of peak response. Arrowheads indicate peak times for the concentrations indicated by different shading. (**C$_2$**) Peak firing rate of odor-evoked activity for all cell-odor pairs is independent of concentration. (**C$_3$**) Peak time of odor-evoked activity for cell-odor pairs is concentration dependent. (**C$_4$**) Pairwise peak time differences between neurons indicates that odor-evoked firing in CA1 becomes more synchronous as odor concentration is increased. Error bars represent SEM.

Supplemental information

Parallel pathways for rapid odor processing in lateral entorhinal cortex: rate and temporal codes by layer 2 subcircuits

Sebastian H Bitzenhofer et al.

Document S1. Figures S1-S7

Figure S1, related to Figure 1

Figure S2, related to Figure 2

Figure S3, related to Figure 3

Figure S4, related to Figure 4

Figure S5, related to Figure 5

Figure S6, related to Figure 6

Figure S7, related to Figure 7

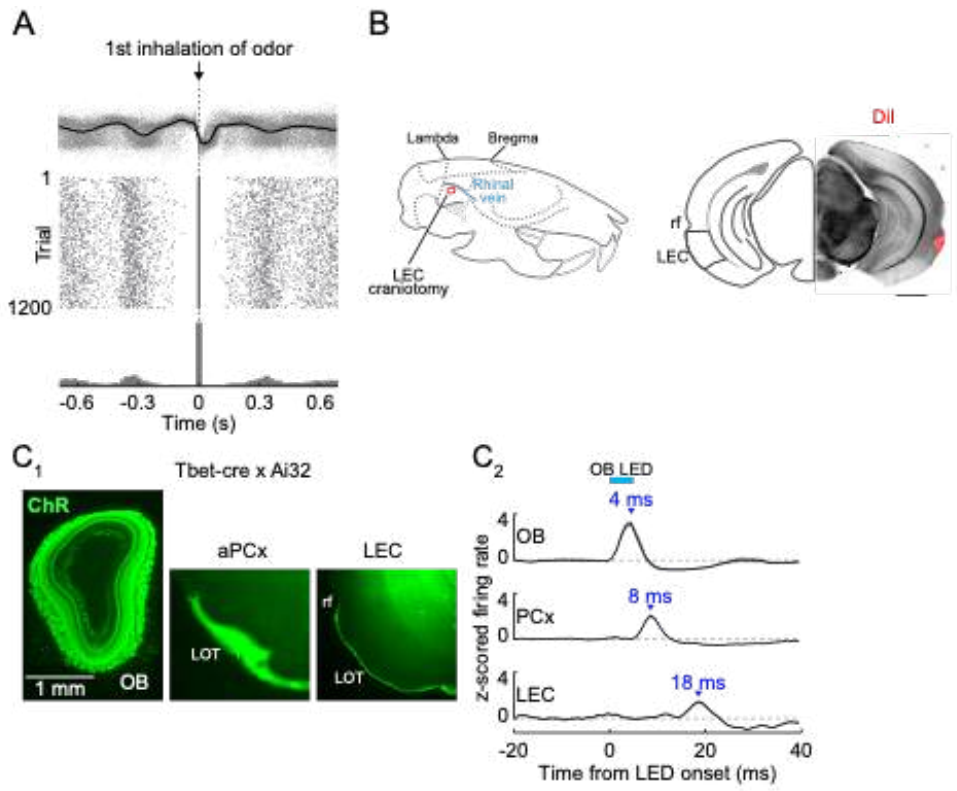

Supplemental Figure 1, relates to Figure 1.

(**A**) Isolation of first inhalation during odor application, Top, respiration traces (grey) for individual trials from one experiment aligned to the first inhalation during odor delivery. Black trace, average of all trials. Middle, raster plot of inhalation onset times for each trial. Bottom, peristimulus time histogram of inhalation onset times from trials.

(**B**) Identification of LEC site for in vivo recording. Left, schematic illustrating the position of the craniotomy over LEC. Right, image of a coronal brain slice showing the recording site labeled with DiI. Scale bar, 1 mm.

(**C**) Optogenetic activation of mitral cells illustrates the minimal time course for propagation of signalling from OB. (**C_1**) Sections from Tbet-cre x Ai32 mouse showing ChR2/GFP expression in OB mitral cells and LOT fibers of PCx and LEC. (**C_2**) Averaged firing rate of single cells recorded from OB (n=12 cells, 2 recordings), PCx (n=171 cells), and LEC (n=59 cells) in response to 5 ms LED illumination (473 nm) over the OB.

Error bars represent SEM.

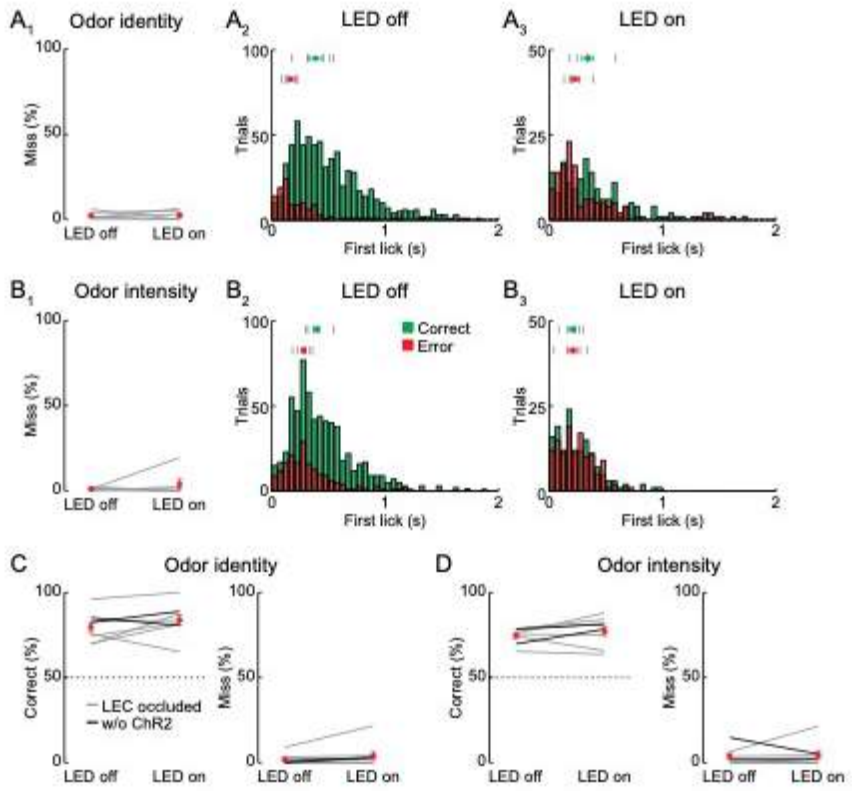

Supplemental Figure 2, relates to Figure 2.

(**A**) LEC silencing during 2AFC odor identity discrimination does not alter miss rate or response timing. (**A_1**) Percent of miss trials in the 2AFC with and without optogenetic silencing of the LEC during all experiments (n=6 mice). Grey lines, individual experiments. Red circle, mean ±SEM. (**A_2**) Histograms of time to first lick for correct (green) and error (red) trials with LED off. Tick marks indicate average response times for individual mice (top, Correct; bottom, Error). Green circle, timing of correct responses averaged across mice (±SEM). Red circle, timing of error responses averaged across mice (±SEM). (**A_3**) As in A_2 for LED on trials.

(**B**) LEC silencing during 2AFC odor intensity discrimination does not alter miss rate or response timing (n = 6 mice). (**B_1** – **B_3**) As described for A.

(**C**) Control experiments for LEC silencing during odor identity discrimination. Left, percent of correct choices during sham optogenetic silencing of the LEC (n=8 mice). Grey lines, same mice from experiments above but with the LEC masked from LED illumination (LEC occluded). Black lines, GAD2-cre mice trained in the task but uninjected with AAV-ChR2. Right, percent of miss trials during sham silencing. Red symbols, average ±SEM.

(**D**) Control experiments for LEC silencing during odor intensity discrimination (n = 8 mice). As described for C.

Error bars represent SEM.

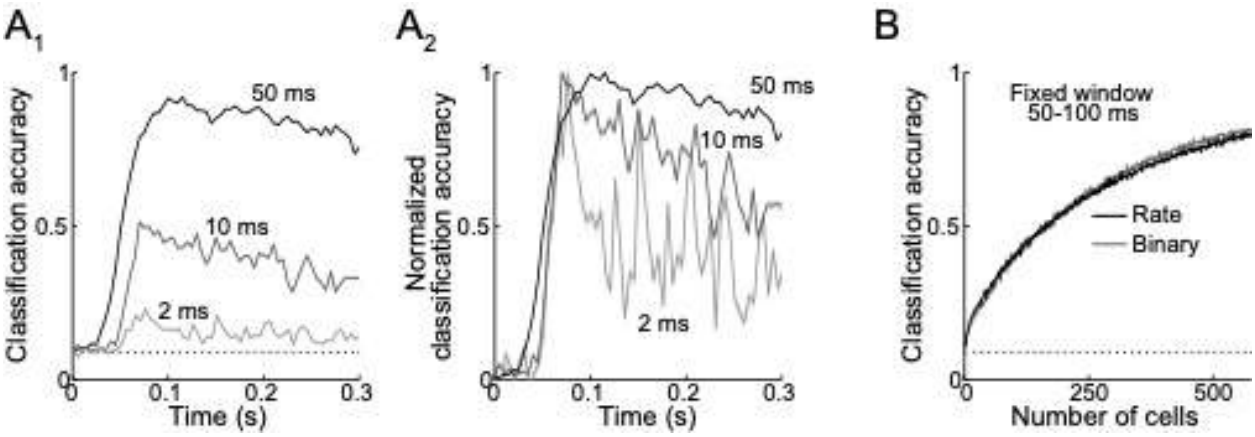

Supplemental Figure 3, relates to Figure 3.

(**A**) Classifier accuracy is highest during early periods of the odor response. (**A_1**) Reducing bin size from 50 to 10 and 2 ms for measurements of classifier accuracy of odor identity makes accuracy course more transient. Dotted line, chance. (**A_2**) Same as (A_1) but baselined to chance and scaled to peak accuracy.

(**B**) Classification accuracy as a function of ensemble size is identical using firing rate or binary measure of activity in a fixed window at 50-100 ms.

Error bars represent SEM.

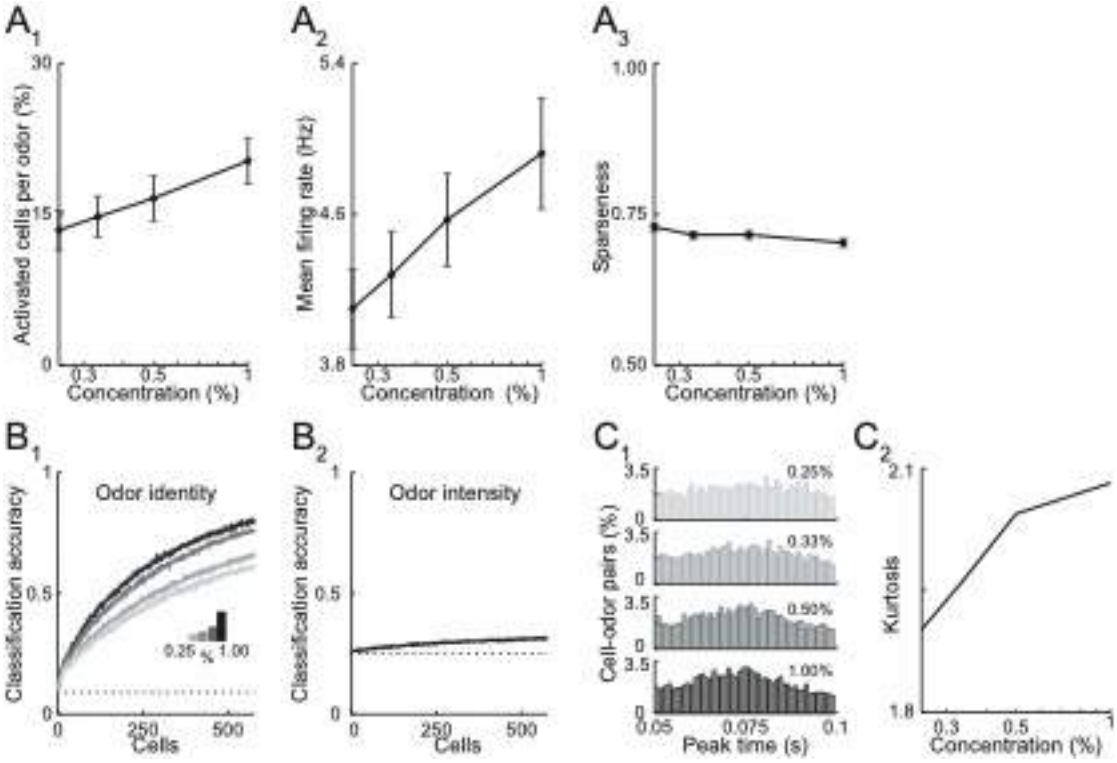

Supplemental Figure 4, relates to Figure 4.

(**A**) Summary data describing effects of odor concentration on responses in LEC L2. (**A$_1$**) Percent of activated cells per odor (rate during 50-100 ms window post-inhalation) at different intensities. (**A$_2$**) Mean firing rate at each concentration for all cell-odor pairs. (**A$_3$**) Lifetime sparseness of odor identity for the four different concentrations.

(**B**) Odor identity vs. odor intensity rate coding as a function of ensemble size. (**B$_1$**) Odor identity classification accuracy using mean firing rate at different intensities (fixed window 50-100 ms post-inhalation). (**B$_2$**) Odor intensity classification accuracy using same measure.

(**C**) Activity becomes more synchronized as odor concentration increases. (**C$_1$**) Peak time histograms of odor-evoked activity at different intensities for all cell-odor pairs. (**C$_2$**) Kurtosis of the peak time distributions shown in (C$_1$).

Error bars represent SEM.

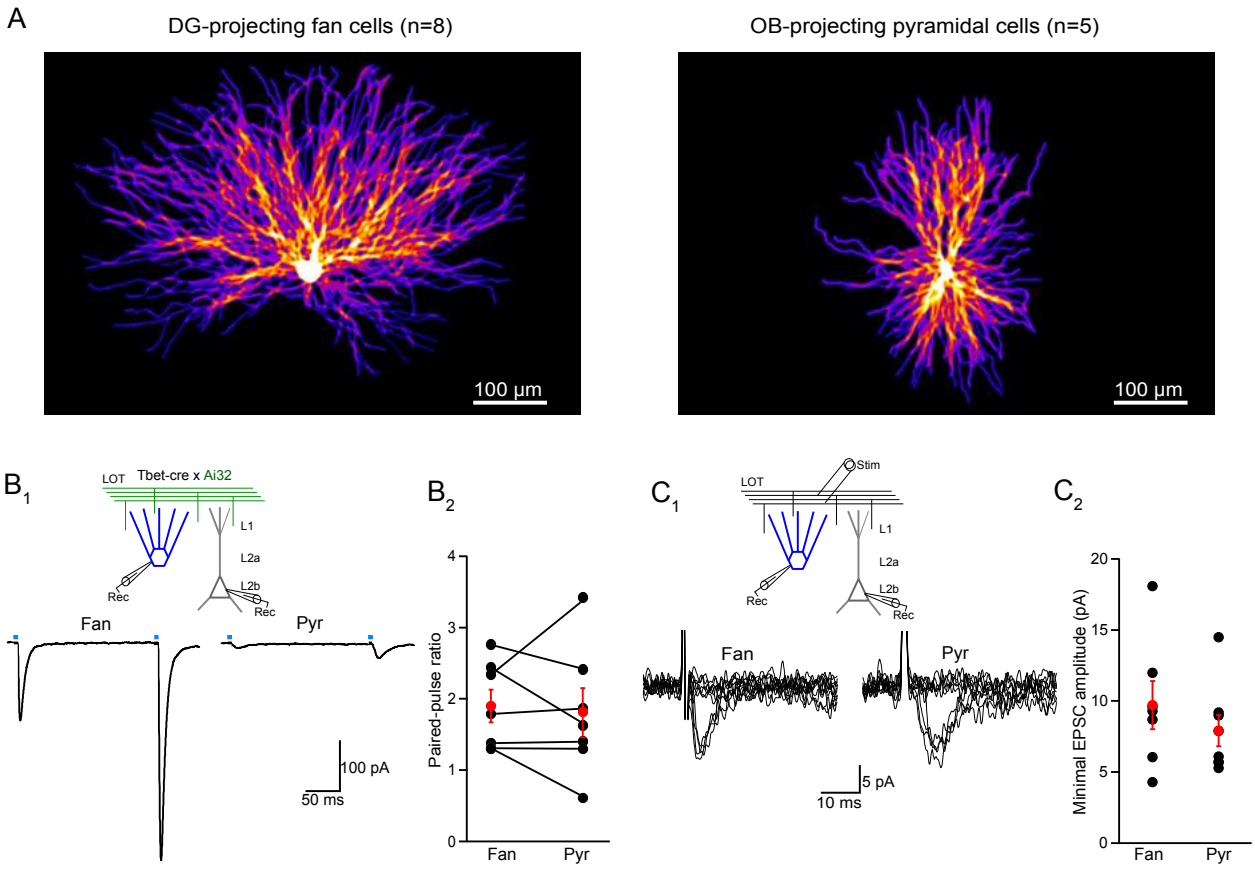

Supplemental Figure 5, relates to Figure 5.

(**A**) The dendritic arbors of LEC fan cells take up more cortical space than pyramidal cells. Left, heat map of reconstructed DG-projecting LEC L2 fan cells (n=8 cells). Image shows average of all cells superimposed. Brighter colors indicate more overlap of dendrites across cells. Right, same for LEC L2 pyramidal cells (n=5 cells).

(**B**) Paired-pulse ratios of LOT-evoked EPSCs onto fan and pyramidal cells suggest synapses of both cell types have similar release probabilities. (**B_1**) Top, recording schematic for paired whole cell recordings of LEC L2 fan and pyramidal cells and optogenetic stimulation (4 ms) of the LOT input. Bottom, representative EPSCs elicited by paired-pulse stimulation (interstimulus interval, 200 ms). (**B_2**) Paired-pulse ratio of responses from paired recordings. Black circles and lines, individual cell pairs. Red circles, mean ±SEM.

(**C**) Minimal LOT stimulation indicates that fan and pyramidal cells have similar single fiber responses. (**C_1**) Top, recording schematic showing LOT minimal electrical stimulation. Bottom, overlay of superimposed trials (n=10) showing failures and successes recorded in a fan (left) and pyramidal cell (right) using threshold stimulation. (**C_2**) Summary of minimal EPSC amplitude (average of success) in fan and pyramidal cells (n=7 and 6, respectively). Black circles, individual recordings. Red circles, mean ±SEM.

Error bars represent SEM.

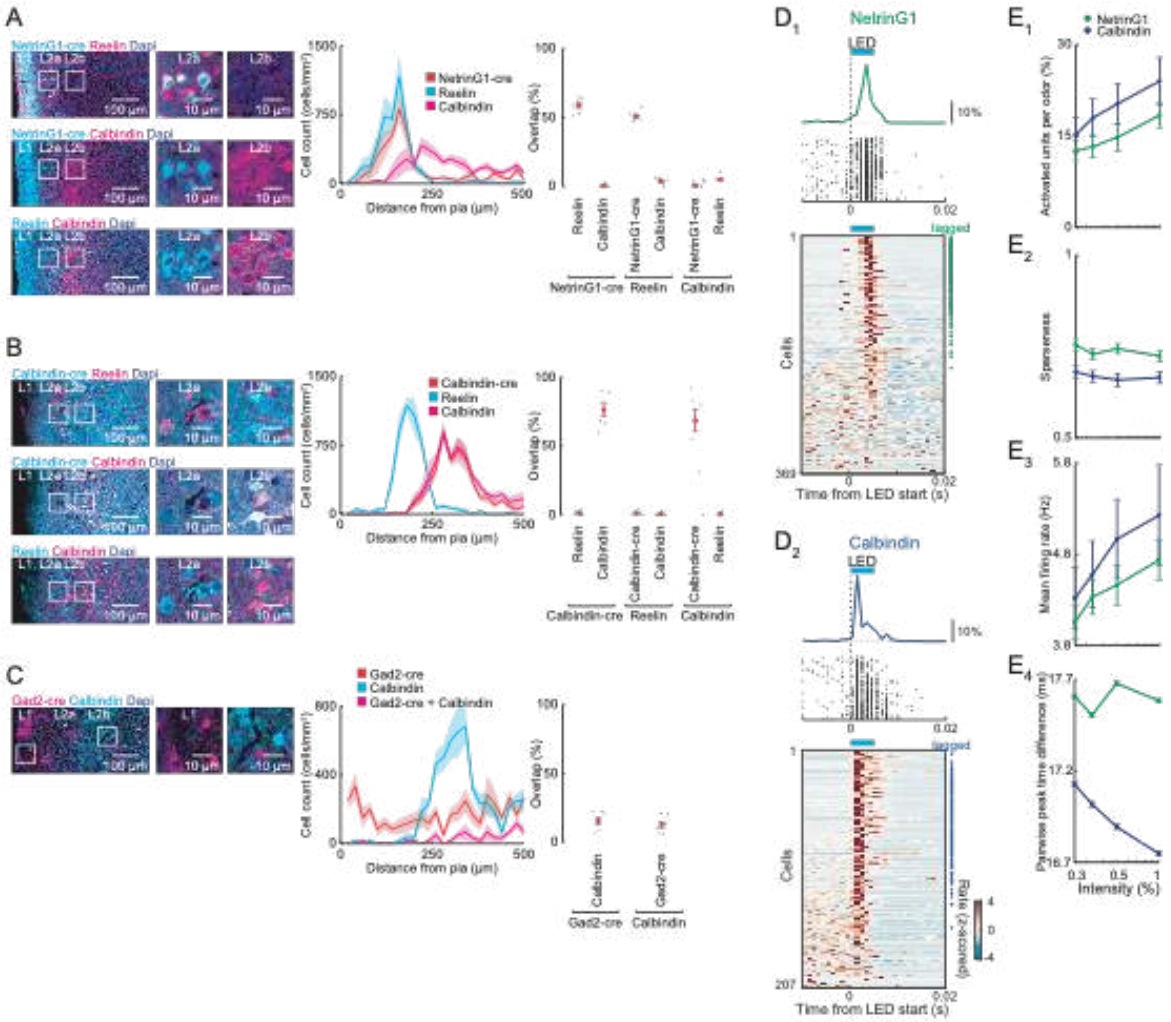

Supplemental Figure 6, relates to Figure 6.

(**A**) NetrinG1-cre labeling of fan cells. Left, coronal sections of LEC from mice expressing tdTomato in cre^{+} neurons immunostained for Reelin and Calbindin. Center, locations of labeled neurons (n=6 slices, 3 mice). Right, percent overlap between labelled neurons in L2 (n=6 slices from 3 mice).

(**B**) Calbindin-cre labeling of pyramidal cells. Left, coronal sections of LEC from mice expressing tdTomato in cre^{+} neurons immunostained for Reelin and Calbindin. Center, locations of labeled neurons (n=6 slices, 3 mice). Right, percent overlap between labelled neurons in L2 (n=6 slices, 3 mice).

(**C**) Only a small fraction of Calbindin-expressing cells in LEC L2 are GABAergic. Left, representative images of LEC L2 from coronal sections of mice expressing tdTomato in Gad2-positive neurons immunostained for Calbindin. Center, distance of labeled neurons from the pia (n=6 slices from 3 mice). Right, percentage of overlap between labelled neurons in LEC L2 (n=6 slices from 3 mice).

(**D**) Optogenetic tagging of ChR2-expressing neurons in NetrinG1- and Calbindin-cre mice. (**D$_1$**) Single units identified as fan cells in NetrinG1-cre mice. Top, spike raster and PSTH from a ChR2-expressing cell responding to LED illumination (5 ms, 473 nm). Bottom, plot of all L2 cells recorded during phototagging experiments rank ordered by LED-evoked firing rate. Symbols at right indicate cells meeting tagging criteria (see Methods). (**D$_2$**) Single units identified as L2 pyramidal cells in Calbindin-cre mice as in D$_1$.

The longer latency for activation of NetrinG1 cells may reflect lower levels of ChR2 expression compared to pyramidal cells.

(**E**) Summary of Netrin-cre/fan and Calbindin-cre/pyramidal cell responses to different odor concentrations (50-100 ms post-inhalation). (**E$_1$**) Percent of activated NetrinG1 (green) and Calbindin (purple) cells. (**E$_2$**) Lifetime sparseness of odor-evoked activity. (**E$_3$**) Mean firing rate of odor-evoked activity all cell-odor pairs. (**E$_4$**) Mean pairwise peak time difference of odor-evoked activity at different intensities for all cell-odor pairs.

Error bars represent SEM.

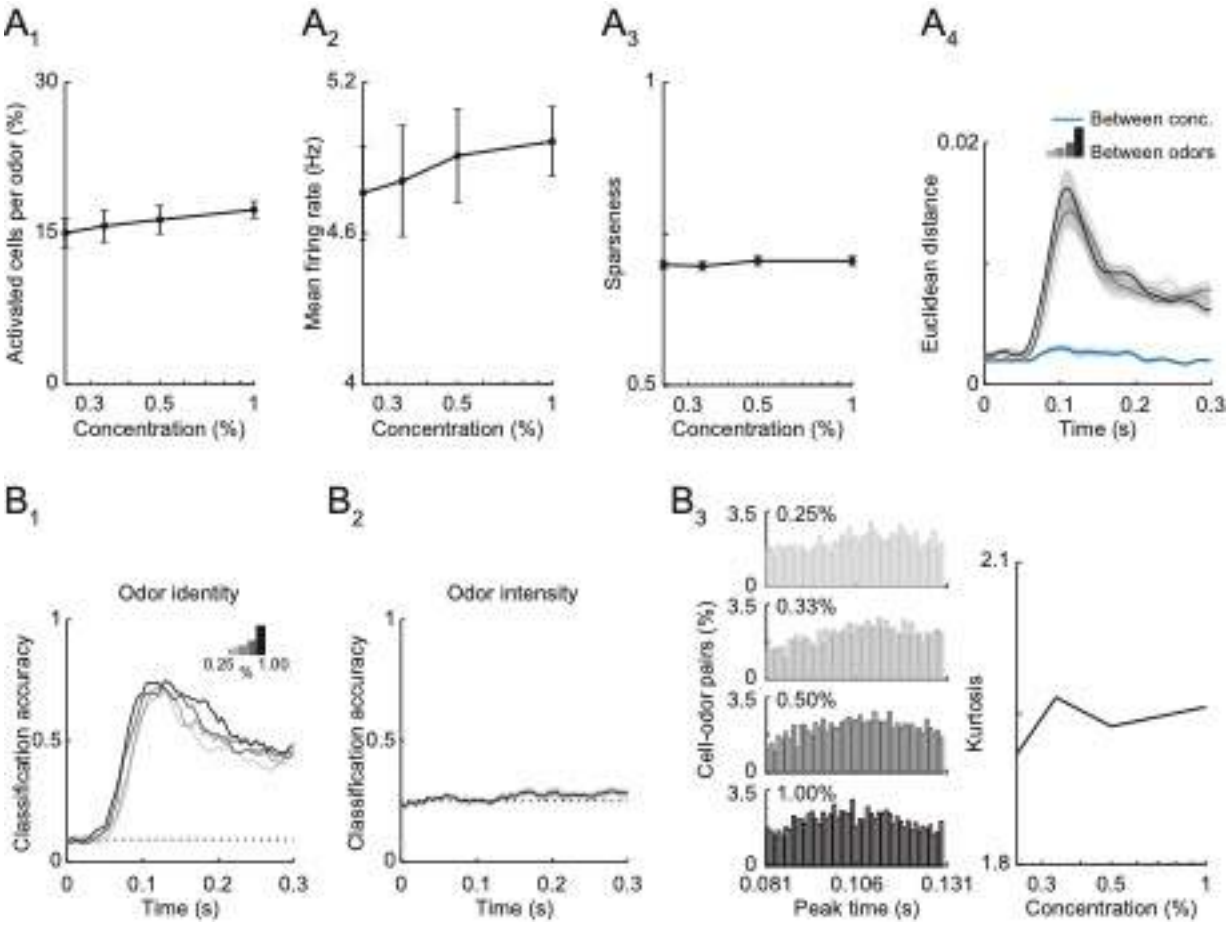

Supplemental Figure 7, relates to Figure 7.

(**A**) Summary of CA1 responses to odor concentrations (81-132 ms post-inhalation). (**A$_1$**) Percent of activated cells per odor. (**A$_2$**) Mean firing rate of odor-evoked activity for all cell-odor pairs. (**A$_3$**) Lifetime sparseness of odor-evoked activity. (**A$_4$**) Euclidean distance of the first three principal components of odor evoked activity between 11 odors (gray to black) at the different concentrations (binned with 1 ms time window). Blue line indicates Euclidean distance between intensities for any given odor.

(**B**) Linear classifier performs well using CA1 firing rate to decode odor identity but performs poorly decoding odor intensity (**B$_1$**) Classification accuracy for odor identity at different intensities (0.25, 0.33, 0.50, 1.00%) based on average firing rate (50 ms sliding window with 5 ms steps). (**B$_2$**) Classification accuracy of odor intensity for all 11 odors based on average firing rate. (**B$_3$**) CA1 activity becomes more synchronized as odor concentration increases. Left, peak time histograms of odor-evoked activity at different intensities for all cell-odor pairs. Right, kurtosis of the peak time distributions shown at left.

Error bars represent SEM.